REVISION 2

The infrared vibrational spectrum of andradite-grossular solid solutions. A quantum-mechanical simulation

MARCO DE LA PIERRE,[1,*] YVES NOËL,[2] SAMI MUSTAPHA,[3] ALESSIO MEYER,[1] PHILIPPE D'ARCO,[2] AND ROBERTO DOVESI[1]

[1]*Dipartimento di Chimica, Università di Torino and NIS, Nanostructured Interfaces and Surfaces, Centre of Excellence, Via P. Giuria 7, 10125 Torino, Italy*

[2]*Institut des Sciences de la Terre de Paris (UMR 7193 UPMC-CNRS), UPMC, Sorbonne Universités, Paris, France*

[3]*Centre de Mathématiques de Jussieu (UMR 7193 UPMC-CNRS), UPMC, Sorbonne Universités, Paris, France*

ABSTRACT

The IR vibrational spectra of andradite-grossular ($Ca_3Fe_2Si_3O_{12}$ – $Ca_3Al_2Si_3O_{12}$) solid solutions were simulated at the *ab initio* level with the CRYSTAL09 code by using a large all-electron Gaussian-type basis set and the B3LYP hybrid functional. All the 23 symmetry independent configurations resulting from the substitution of 1 to 8 Fe atoms with Al atoms in the *16a* octahedral site of the andradite primitive cell were considered. The IR active transverse optical frequencies and their intensities were computed. Graphical representation of the spectra, animation of the modes and isotopic substitution of the cations were used as additional interpretation tools. The dominant high frequency modes, corresponding to Si-O stretching motions, show a simple linear behavior of both frequencies and intensities with respect to the binary composition; this trend is related to the linear behavior of the mean lattice parameter. Also the frequencies of the low energy bands show, roughly speaking, a linear dependence on composition; however, the behavior of the dominant intensities is more complicated and strongly connected to the Al and Fe atomic fraction. When considering different possible structures at fixed composition, the spectral features show a dependence upon short range cation ordering.

Keywords garnets, andradite, grossular, solid solutions, IR frequencies, IR intensities, ab initio calculations, all electron gaussian basis sets, B3LYP, CRYSTAL code

[*] E-mail: *marco.delapierre@unito.it*

INTRODUCTION

Garnets ($X_3Y_2Si_3O_{12}$) are important rock-forming silicates, as major constituents of the Earth's upper mantle and relevant phases of high-pressure metamorphic rocks in the Earth's crust (Deer et al. 1992). From the technological point of view, they are largely used for a variety of industrial applications, for example filtration media and abrasives, thanks to their recyclability and high hardness (Olson 2001). The SiO_4 tetrahedra are the building blocks of the structure, interconnected with YO_6 octahedra, whereas the X^{2+} cations fill the dodecahedral cavities. The highly symmetric $Ia\bar{3}d$ space group contains 48 point-symmetry operations.

Natural garnets rarely exist as pure end members. They rather form solid solutions extending over a broad chemical range involving up to 12 end members (Rickwood 1968). The most common cases refer to substitutions of trivalent cations at Y sites or divalent cations at X sites. Simultaneous substitutions at X and Y sites can also be observed. Intermediate compositions have been the object of extensive studies, and a large set of experimental data is currently available, including structural refinements (Merli et al. 1995), thermal expansion and elasticity (Isaak and Graham 1976; Isaak et al. 1992; O'Neill et al. 1989), birefringence (Hofmeister et al. 1998; Akizuki 1984; Andrut and Wildner 2001; Wildner and Andrut 2001) and Raman spectra (Kolesov and Geiger 1998).

Many investigations on silicon (McAloon and Hofmeister 1995; Hofmeister et al. 1996, 2004; Geiger et al. 1989; Geiger 1998; Kolesov and Geiger 1998), aluminium (Chiriu et al. 2006) and gallium (Papagelis et al. 2010) garnets dealt with the infrared (IR) response. In these studies the effect of chemical substitution was investigated, and the dependence of the spectrum on the composition (and cell volume) was interpreted on the basis of simple linear models, namely one- and two- mode behaviors (Lucovsky et al. 1968; Chang and Mitra 1968; Fertel and Perry 1979), which rely on the hypothesis of ideal mixing of the end members. However, several issues hinder a full understanding of the experimental data: instrumental accuracy, correlation among model parameters in the Kramers-Kronig analysis, proper symmetry analysis of the binary compounds, hypothesis on mode decoupling, uncertainty on composition and structural distribution of cations.

In the context of solid solutions, computational techniques can be applied for a more detailed analysis. Semi-classical models (Bosenick et al. 2000; Becker and Pollok 2002; van Westrenen et al. 2003; Vinograd et al. 2004; Vinograd and Sluiter 2006; Vinograd et al. 2006) have been the highest level of theory applicable to these problems for a long time. However, papers based on *ab initio* DFT methods applied to pyrope-grossular (Sluiter et al. 2004; Freeman et al. 2006) and pyrope-majorite (Yu et al. 2011) solid solutions have been published recently. In these studies the computed energies were used within a Cluster Expansion Method (CEM) scheme (Connolly and Williams 1983; Laks et al. 1992; Sluiter and Kawazoe 2003; Vinograd et al. 2004), the main goal being the investigation of the thermodynamic properties of the solid solution.

Regarding garnets, quantum mechanical methods were successfully used to compute the vibrational properties (frequencies and intensities), dielectric constants, IR reflectance spectra and magnetic properties of pure garnet end members (Pascale et al. 2005; Zicovich-Wilson et al. 2008; Dovesi et al. 2011; Meyer et al. 2010), including grossular ($Ca_3Al_2Si_3O_{12}$, indicated as Grs in the following) and andradite ($Ca_3Fe_2Si_3O_{12}$, Adr). Structural and thermodynamical properties of the andradite-uvarovite binary were also investigated with the same approach (Meyer et al. 2009).

In this paper we extend the analysis to the IR vibrational spectrum of andradite-grossular (Adr-Grs) solid solutions. We investigate the dependence of the spectrum on the parameters characterizing the Adr-Grs binaries: composition, structural parameters (in turn related to cations chemistry), interactions among cations occupying the Y sites. The resulting representation of the evolution of the IR spectrum, in going from one end member to the other, will provide clues for the critical interpretation of the experimental findings. To our knowledge, this is the first *ab initio* study of the infrared properties of a garnet solid solution.

MODELING APPROACH

Computational details

As in previous studies on end member garnets (Pascale et al. 2005; Zicovich-Wilson et al. 2008;

Dovesi et al. 2011; Meyer et al. 2010), the hybrid B3LYP spin-Hamiltonian (Becke 1993), all-electron Gaussian type basis sets and the CRYSTAL09 code (Dovesi et al. 2009) were used. B3LYP is widely and successfully used in molecular quantum chemistry (Koch and Holthausen 2000) as well as in solid state calculations, where it was shown to provide equilibrium geometries, vibrational frequencies (Pascale et al. 2005; Zicovich-Wilson et al. 2008; Dovesi et al. 2011; Zicovich-Wilson et al. 2004; Prencipe et al. 2004; Demichelis et al. 2011) and magnetic properties such as the super-exchange coupling constants (Moreira et al. 2002; Moreira and Dovesi 2004; Muñoz et al. 2004; Patterson 2008; Meyer et al. 2010) in good agreement with experimental data.

As regards the basis set, oxygen, silicon, calcium, aluminium and iron were described by (8s)(411sp)(1d) (Pascale et al. 2005), (8s)(6311sp)(1d) (Pascale et al. 2005), (8s)(6511sp)(3d) (Pascale et al. 2005), (8s)(611sp)(1d) (Zicovich-Wilson et al. 2008) and (8s)(64111sp)(411d) (Pascale et al. 2005) contractions, respectively. For the discussion of the computational conditions (tolerances for the truncation of the infinite Coulomb and exchange sums, SCF convergence criteria, grid size for integration of the exchange-correlation density functional and number of points in the reciprocal space) we refer to our previous studies on garnets (Pascale et al. 2005; Zicovich-Wilson et al. 2008; Dovesi et al. 2011; Meyer et al. 2010), where the effect of the basis set size on various properties was also investigated. Examples of input and output files can be retrieved from the CRYSTAL web site (www.crystal.unito.it/supplement/index.html).

Structure optimizations were performed by using the analytical energy gradients with respect to atomic coordinates and unit-cell parameters (Doll 2001; Doll et al. 2001; Civalleri et al. 2001), and a Broyden-Fletcher-Goldfarb-Shanno scheme for Hessian updating (Broyden 1970; Fletcher 1970; Goldfarb 1970; Shanno 1970). Convergence was checked on both the gradient components and the nuclear displacements (TOLDEG and TOLDEX, see Dovesi et al. 2009, were set to $3.0 \cdot 10^{-5}$ Ha/Bohr and $1.2 \cdot 10^{-4}$ Bohr, respectively).

Point symmetry was used as extensively as possible. Symmetry lowering of intermediate Adr-Grs configurations implies higher computational costs for the SCF cycle and a larger number of degrees of freedom to be optimized, with a consequent increase of the number of optimization steps. For example, when symmetry drops from 48 (end members) to 2 point-symmetry operators (lowest symmetry mixed composition), the cost of a single SCF cycle increases from 50 to 800 seconds, and the number of optimization steps from 8 to 76 (timings refer to a DIRECT strategy, see Dovesi et al. 2009, and parallel running on a cluster of eight standard Intel Core2 CPUs).

The calculation of the transverse optical (TO) vibrational frequencies ν_0 at the Γ point was performed within the harmonic approximation. The mass-weighted Hessian matrix is constructed by numerical differentiation of the analytical gradients with respect to the atomic cartesian coordinates; one calculation would then require (3N + 1) SCF+gradient calculations (241 for our unit cell, containing N = 80 atoms). However, symmetry reduces this number to between 9 (end members) and 133 (lowest symmetry cases). The calculation of the vibrational spectrum for a configuration with the lowest symmetry requires about one month on the 8-CPUs node mentioned above.

Infrared intensities I_p were computed for each p^{th} mode by means of the mass-weighted effective mode Born charge $\vec{Z}_p$ (Barrow 1962; Hess et al. 1986), evaluated through a Berry phase approach (Dall'Olio et al. 1997; Noël et al. 2002):

$$I_p = \frac{\pi}{3}\frac{N_A}{c^2} \cdot d_p \cdot \left| \frac{\partial}{\partial Q_p} \vec{\mu} \right|^2 \tag{1}$$

$$\left| \frac{\partial}{\partial Q_p} \vec{\mu} \right|^2 = \left| \vec{Z}_p \right|^2 = \left(Z_{p,x}^2 + Z_{p,y}^2 + Z_{p,z}^2 \right) \tag{2}$$

where N_A is the Avogadro's number, c is the speed of light, d_p is the degeneracy of the p^{th} mode, $\vec{\mu}$ is the cell dipole moment, Q_p is the normal mode displacement coordinate, $\vec{Z}_p$ is the Born charge vector in the basis of the normal modes. Further details on the calculation of vibrational frequencies can be found in Pascale et al. 2004; Zicovich-Wilson et al. 2004; Zicovich- Wilson et al. 2008.

A graphical representation of the infrared spectrum $S_L(\nu)$ for each configuration L was obtained as a superposition of Lorentzian functions F, one for each mode:

$$S_L(\nu) = \sum_p F(\nu; \nu_{0,p}, I_p, \gamma_p) \quad (3)$$

$$F(\nu; \nu_{0,p}, I_p, \gamma_p) = \frac{I_p}{\pi}\left[\frac{\gamma_p/2}{(\nu-\nu_{0,p})^2 + (\gamma_p/2)^2}\right] \quad (4)$$

where γ_p is the damping factor of the pth mode, which is related to the phonon lifetime. Being unable to compute this quantity, we used a constant value of 9 cm^{-1}, already adopted in Dovesi et al. 2011 to simulate the reflectance spectra of six garnets. $S_L(\nu)$ curves were evaluated in the range 100-1000 cm^{-1}, in steps of 1 cm^{-1}.

When several configurations exist with a given composition *x*, the reported spectrum $\bar{S}_x(\nu, T)$ was obtained as a weighted average over all the corresponding spectra $S_L(\nu)$, by using the Boltzmann occupation probabilities $\mathcal{P}_L$ at temperature T= 1300 K and cell volume V as obtained upon structure optimization (for a given composition, V turns out to be constant to within 0.05 %, see Table 1):

$$\bar{S}_x(\nu, T) = \sum_L^{\text{fixed x}} P_L(V,T) \cdot S_L(\nu) \quad (5)$$

$$P_L(V,T) = \left(\frac{M_L}{\sum_L^{\text{fixed x}} M_L \cdot e^{-\frac{E_L(V)}{k_B T}}}\right) e^{-\frac{E_L(V)}{k_B T}} \quad (6)$$

where $E_L(V)$ is the total energy of the L^{th} configuration, including the vibrational zero-point energy; $\mathcal{M}_L$ is the multiplicity of the L^{th} configuration (see Table 1 for $\mathcal{M}_L$ and $\mathcal{P}_L$ at 1300 K; $E_L(V)$ reported in the Supplementary Material). Note that at 1300 K a single configuration provides more than 50% of the total weight for all but x_{Al} = 0.5 compositions. At 300 K this number increases to 80% (see Supplementary Material).

Graphical animation of the normal modes permits a visual reading of the corresponding eigenvectors. It is available for end member configurations at the CRYSTAL web site (www.crystal.unito.it/prtfreq/jmol.html), and permits a direct interpretation of the "nature" of the mode (stretching, bending, rotation of the tetrahedra, translation of the X^{2+} cation, etc.) by simple and intuitive means.

Structural model

The size of the reference cell has relevant effects on the description of the solid solution. In particular, it affects the number of atomic distributions (configurations), the set of accessible compositions, the order of the stars of neighbour pairs that can be populated independently. In order to limit the computational cost (already quite high), the rhombohedral primitive cell of the end members was taken as a reference in this study; it contains 8 trivalent Y cations (Y can be Fe and/or Al) lying on a set of equivalent 16*a* octahedral sites. Figure 1 reports a schematic representation of the octahedral sites in the structure of garnets: both the primitive and the cubic conventional cells (80 and 160 atoms in total, respectively) are shown; the primitive cell Y sites contained in the conventional cell are shaded and labelled from 1 to 8; translationally equivalent sites in the conventional cell are labelled with primes.

Nine discrete compositions were considered, by varying the number of Al atoms substituting Fe atoms in the Y sites from 0 to 8 (the atomic fraction x_{Al} of Al atoms then ranges from 0 to 1, in steps of 0.125). Considering 2 chemical species distributed over the 8 sites, $2^8 = 256$ configurations are possible. This set can be partitioned in classes of symmetry-equivalent configurations. A symmetry analysis, carried out as described in Mustapha et al. 2012, shows that there are 23 such classes. Among these, 2 correspond to the end members, Adr and Grs, the remaining 21 to intermediate binaries. Pairs of Y cations can be populated independently up to the second neighbours (i.e. up to a pair distance of 6.097 and 5.980 Å in Adr and Grs, respectively).

Table 1 summarizes the structural and symmetry information for the 23 symmetry independent (classes of) configurations. Garnet end members show 48 symmetry operators ($\mathcal{S}$ in the Table); upon substitution in the Y site, this number spans from 24 (the configuration at $x_{Al} = 0.5$ with the highest symmetry) to 2 (the least symmetric configurations). As the symmetry reduces, the multiplicity $\mathcal{M}$ of each configuration increases, as well as N_{df}, the number of degrees of freedom to be considered in the structure optimization process.

The crystalline system ranges from cubic (end members) to triclinic (lowest symmetry), even if in every case a quasi-cubic structure is easily identified, as reported in Table 1. Indeed, deviations from the cubic metric are small and compare favorably to the experimental structures of "non-cubic" garnets (McAloon and Hofmeister 1995). Figure 2 shows that the cubic root of the cell volume $\bar{a}$ (that coincides with the lattice parameter in the case of cubic systems) decreases linearly from Adr to Grs, with a slope of -0.029 Å per site substitution (in the primitive cell), very similar to that obtained from experiments in McAloon and Hofmeister 1995 (-0.027 Å per site substitution).

RESULTS AND DISCUSSION

Vibrational properties: general features

Frequencies and intensities of the IR vibrational modes were computed at the *ab initio* level for the 23 symmetry independent configurations. The most significant quantities are summarized in Table 2, in Figure 3 (providing the spectra of the seven independent configurations at x_{Al} = 0.5) and in Figure 4, showing the weighted-average spectra for the various compositions from Adr to Grs, in steps of 0.125.

As the symmetry reduces, the number of allowed IR active modes (N_{IR} in Table 2) increases and the spectra become more complicated: there are 17 modes in the end members, 33 in the x_{Al} = 0.5 configuration with highest symmetry, and 129 in configurations with 2 symmetry operators only. The additional allowed modes have intensities that are somehow proportional to the distortion from the original cubic symmetry.

For convenience, the spectral range was divided in two regions, i.e. below (Lν) and above (Hν) 700 cm^{-1} (L and H stand for low and high frequency). Modes in the Hν region are related to stretching motions of the SiO_4 tetrahedra, whereas Ca and Fe/Al cations provide important contributions to the Lν modes (see the "type" column in Table 2). These attributions were obtained by combining graphical animation of the modes with isotopic substitution (see Figure 5, which will be discussed in the "IR wavenumbers" Section).

In the following, we will simplify the discussion by focusing on the dominant features of the infrared spectra. The end members (see Figure 4) show four very intense bands with maxima at 277.8, 363.9, 792.4 and 866.9 cm^{-1} (Adr), and at 386.3, 432.7, 827.8 and 900.6 cm^{-1} (Grs). When moving to binary systems, active modes (three-fold degenerate, F_{1u} symmetry) split, and many others become active. As regards the high frequency Hν region, up to 15 and 8 modes appear in the binaries (L14 configuration) in the frequency ranges of the 792.4 and 866.9 cm^{-1} bands of Adr, respectively (the end member shows only 2 and 1 modes). However, the convolution of such large sets of modes in the binaries nearly coincides with the two bands of the end members. When considering the low frequency Lν region, for lowly substituted binaries (1-2 atoms) the convolution of the IR active modes still results in two well-defined spectral features. In highly substituted binaries (3-5 atoms) the 290 (x_{Al} = 3) - 380 (x_{Al} = 5) cm^{-1} range shows a large number of modes of similar intensity (24 in the case of L14), which makes the identification of bands more difficult and the correspondence with the end members looser, whereas a well-defined feature is still found in the 370 (x_{Al} = 3) - 440 (x_{Al} = 5) cm^{-1} range (including up to 13 modes in L14). In the following, we will call IR bands the four sets of features along the solid solution series described above, which mimic the four intense structures in the end members spectra; they are labelled as Lν(1), Lν(2) and Hν(3), Hν(4), respectively.

Each band is attributed the frequency of its most intense mode ("ν" in Table 2). The integrated intensity ("II" in the Table) of the four bands shows a very regular trend along the series from one end member to the other, indicating that II is a significant quantity for our investigation. For each band, II is the sum of the intensities I of all modes within the corresponding band range; note that, given the high number of modes of similar intensity in highly substituted binaries (3-5 atoms), an uncertainty in the order of a few hundreds km/mol should be considered for II values. For a more detailed definition and description of IR bands and related quantities, see Supplementary Material.

IR wavenumbers

Figure 6(a) (and Table 2) shows that the frequencies of Hν(3) and Hν(4) bands (stretching modes of the SiO4 tetrahedra) vary linearly from one end member to the other. ν(3) increases from 792.4 (Adr) to 827.8 (Grs) cm^{-1} ($\Delta\nu_{1\text{-}23}$ = 35.4 cm^{-1}). The best fit straight line is ν(3) = (789.3 + 4.6 · n_{Al}) cm^{-1}, the maximum deviation from the linear behavior being 3.6 cm^{-1} (in only 3 cases the deviation is larger than 2.3 cm^{-1}, i.e. larger than half the difference between two contiguous compositions). As regards ν(4), the two end members are at 866.9 (Adr) and 900.6 (Grs) cm^{-1}, respectively ($\Delta\nu_{1\text{-}23}$ = 33.7 cm^{-1}). The slope is the same as for ν(3) (the fit function is ν(4) = (868 + 4.6 · n_{Al}) cm^{-1}); the deviations are slightly larger than for ν(3), however they never exceed 5.0 cm^{-1}.

Given the anti-linear dependence of the cell parameter on the composition (Figure 2), the behaviors of the wavenumbers of Hν bands show an anti-correlation with the cell parameter; a similar result was found in the case of end member garnets both from *ab initio* calculations (Dovesi et al. 2011) and experimental measurements (Hofmeister and Chopelas 1991). The reason is that, as the unit cell becomes smaller, the interatomic distances between O atoms of the SiO_4 tetrahedra and the neighboring atoms reduce; thus the potential (electronic and short range repulsion) perceived by the SiO_4 tetrahedra becomes larger, resulting in higher frequencies. The behavior of the two bands is ruled by this common factor (the reduction of the SiO_4 cage), as confirmed by the fact that the slope of the two straight lines is the same.

The bars in Figure 6(a) represent the frequency differences between symmetry independent configurations with the same composition, that are quite small for Hν bands: the difference with respect to the average value (at fixed composition) exceeds 4 cm^{-1} only in three cases, with a maximum deviation of 8.4 cm^{-1}.

The situation is less simple for Lν(1) and Lν(2), because of the important contribution of the Y cations, that are progressively substituted along the series, and whose motion couples to a large extent. Isotopic substitution (see also Dovesi et al. 2011) permits to point out the participation of the various chemical species to the vibrational modes. An extensive analysis was performed for the Lν bands, by operating in three ways: the mass of Ca was increased by 20% (a); the Fe (b) or Al (c) mass was reduced by 20%. In each case the spectrum was recalculated, and superposed to the original one in order to identify the bands that are related to the motion of the three different cations; these spectra are shown in Figure 5 for the nine compositions under study. As already mentioned in the "Vibrational properties: general features" Section, information on the nature of the two bands was summarized in the "type" column of Table 2, too.

The lowest band Lν(1) is dominated by Fe and Al motions in the case of Adr and Grs end members, respectively (see top and bottom spectra in Figure 5); this simple attribution holds also in the case of compositions close to the end members (see x_{Al} = 0.125, 0.25, 0.75, 0.875 spectra in Figure 5). At intermediate compositions (x_{Al} = 0.375 - 0.625) a large number of modes appears in the Lν(1) frequency range (up to 24 in the case of *L*14), which are related to the motion of both cations. In general, modes associated to Al atoms lie at higher frequency (lighter mass) than those associated to Fe; however, the two species appear to couple to a large extent, thus it was not possible to separate the analysis for the two cations within the Lν(1) band.

The other low frequency band, Lν(2), corresponds to Ca motions in the case of pure Adr (top spectrum in Figure 5). However, as far as Al atoms are inserted in the structure, the motion of this relatively light atom couples with Ca. Indeed, a small component of the Lν(2) band appears to be related to Al cations already in the case of x_{Al} = 0.125 (second spectrum in Figure 5); then, from x_{Al} = 0.25 on, the whole band must be associated to mixed motions of both Ca and Al species (see Figure 5).

Let us now analyze the behavior of the frequencies of Lν bands, by taking Figure 6(a) (and Table 2) as a reference; again, a relatively simple behavior is detected. A linear fit provides ν(1) = (278 +

$14.1 \cdot n_{Al}$) cm^{-1} (correlation factor R = 0.962) and $\nu(2) = (373 + 8.0 \cdot n_{Al})$ cm^{-1} (R = 0.963), respectively. The dispersion with respect to the fit is larger than in the case of Hν bands: in 10 and 6 out of 23 cases, respectively, the deviation is larger than half the difference between two contiguous compositions (14.12 and 8.02 cm^{-1}), the largest ones being 16.4 and 9.7 cm^{-1}, respectively. The end members frequencies are at 277.8 and 363.9 cm^{-1} (Adr), and at 386.3 and 432.7 cm^{-1} (Grs), respectively. The step between the two end members $\Delta\nu_{1\text{-}23}$, that was as small as 35 cm^{-1} for the Hν modes, is here much larger: 108.5 and 68.8 cm^{-1}, respectively.

As for the Si-O stretchings (Hν bands), the two Lν frequencies increase along the series; in this case, this seems the combination of two effects: 1) the reduction of the cell volume; 2) the substitution of a heavy atom (Fe) with a lighter one (Al). The latter issue justifies the higher slopes of Lν bands with respect to Hν bands (the latter do not involve Y cations, thus are not affected by its mass). Also the larger slope of Lν(1) with respect to Lν(2) may be explained in terms of the different participation of cations to the vibrations (which was discussed above). In fact, Lν(2) is essentially a Ca motion, which couples to a certain, but limited, extent with Al motion, when the composition approaches the Grs end member; on the other hand, Lν(1) is a pure Y cation motion, thus it is the most affected by the mass variation when spanning from Adr to Grs.

IR intensities

Figure 6(b) (see also Table 2) shows that the band intensity II of three out of four main bands varies linearly with composition. The slope for II(3) is -1270 km/mol per site substitution; the maximum deviation from the fit, 560 km/mol, and the maximum dispersion at fixed composition (see the two horizontal bars in the Figure), 790 km/mol, are then smaller than the intensity difference between two contiguous compositions. This suggests that the intensity of this band could be used as a marker for the composition of the Adr-Grs solid solutions. For II(4) the slope is five times smaller (-260 km/mol per site substitution, with a maximum deviation from the fit equal to 830 km/mol).

The negative slope of both Hν curves is to be related to the reduction of the cell volume along the series. The resulting shortening of the distances between O atoms of the SiO_4 tetrahedra and the neighboring atoms constrains the motion of the tetrahedra, producing a reduction of the dipole moment variation associated to the mode (i.e. of the Born charge vector modulus $\left|\vec{Z}_p\right|$, see Eqs. (1) and (2) in the "Computational details" Section).

As regards the low frequency region, the two bands show a quite different behavior, that can be related to the different participation of the Y cations (as discussed in the "IR wavenumbers" Section). Intensity II(2) shows a large, positive, nearly linear behavior with respect to the composition (the slope is +1380 km/mol per site substitution); the maximum dispersion at fixed composition (see the two horizontal bars in Figure 6(b)) is always smaller than the intensity difference between contiguous compositions. The growing intensity is possibly associated to the important change in the atoms participating in the modes (see the "IR wavenumbers" Section and Figure 5). Let us consider the case of the end members, whose Lν(2) bands are composed by only 1 (Adr) and 2 (Grs) modes (however, in the latter case one mode provides the 99 % of the total band intensity); thus, in this case the band integrated intensity II(2) reduces to the intensity I of either the unique or major component mode. Adr shows a pure Ca mode (top of Figure 5), the corresponding intensity I being 8542 km/mol; Ca^{2+} is a bulky cation, with a radius of 1.12 Å (Shannon 1976) against a cage size (estimated through the mean cation-oxygen distance within the unit cell) of about 2.4 Å. In Grs, on the contrary, both Ca and Al contribute to the mode (bottom of Figure 5), and I is as large as 20044 km/mol. Al^{3+} cations are much smaller than Ca^{2+} (0.54 Å radius, from Shannon 1976, against a cage size of 1.94 Å); the smaller cation/cage size ratio is responsible for larger cation motions, and thus for the larger dipole moment variations (and larger $\left|\vec{Z}_p\right|$ values, see above).

The Lν(1) band shows a more complex behavior. Its intensity II(1) decreases from 16026 (x_{Al} = 0) to about 7000 km/mol (x_{Al} = 0.375) on the Adr side, then it remains almost constant, showing a plateau at about 8000-9000 km/mol on the Grs side. As already discussed, this band is mainly related to the motion of Y cations. By looking at Figure 5, we notice that in the range x_{Al} = 0 - 0.375, Lν(1) is dominated by Fe; the decreasing fraction of Fe in the unit cell implies a reduced contribution to II(1). For compositions $x_{Al} \geq 0.5$, Al and Fe motions couple together in the Lν(1) band. Thus, the decreasing contribution to II(1) coming from Fe cations is compensated by the increasing contribution from Al; as a consequence, the total band intensity II(1) is almost constant in this latter compositional range.

An overall analysis of intensities along the Adr-Grs binary is possible by considering the sum of intensities $F = \sum_j II_j$ for the two spectral ranges, i.e. Lν and Hν, which is represented in Figure 6(c) (see also Table 2). The contribution at high ν shows a linear behavior, with a slope of -1530 km/mol per site substitution. This is not surprising, being the result of the superposition of the trends observed for the Hν(3) and Hν(4) bands, which have already been discussed above. This trend turns out to be dominant also for the F value integrated along the whole spectral range (with a slope of -1390 km/mol per site substitution).

A rather peculiar trend is found in the case of the contribution at low ν, which is almost constant with respect to the composition, the maximum variation being +1104 km/mol along the 23 configurations (+3%). This behavior is possibly related to a sort of compensation between two opposite effects along the binary series: a) the decrease of the cell parameter, which likely implies a reduction of the dipole moment variation (see discussion above for Hν(3) and Hν(4)), and b) the role of the varying chemical composition in the Y sites, which somehow accounts for an increase of the dipole moment of the modes. Concerning the latter point, one of the possible factors could be the reduction of the Y cationic radius in the octahedral site (r_{Fe} = 0.65 Å, r_{Al} = 0.54 Å, from Shannon 1976). Indeed, we observe that the ratio between the Y cation radius and the Y site size (estimated again through the Y-O mean distance) reduces from 0.3173 (Fe, in Adr) to 0.2782 (Al in Grs). Thus, the shortening of cell parameters turns out to be overcompensated by the reduced dimension of the Y cation.

Behavior at fixed composition

In order to analyze the dependence of the IR spectra upon the structure at fixed composition, i.e. upon the ordering of the Y cations, the x_{Al} = 0.5 case, with seven symmetry independent configurations, was considered (see Table 2 and Figure 3).

As anticipated above ("Vibrational properties: general features" and "IR wavenumbers" Sections), Lν(2), Hν(3) and Hν(4) are essentially independent from the relative position of the Y cations: the maximum variation of frequency (Δν) and intensity (ΔII) at fixed composition is 5 cm^{-1} and 10%, respectively, and only minor differences (e.g. small shoulders and satellite peaks) can be observed between the seven spectra.

The Lν(1) band corresponds, on the contrary, to modes with large contributions from the Y cations ("IR wavenumbers" Section). In this case Δν can be as large as 24 cm^{-1} (*L*10 *vs* *L*11), and ΔII can reach 20% (*L*12 *vs* *L*14). The differences in the Lν(1) frequency range of the spectra become then clearly visible (Figure 3).

Let us concentrate the analysis on a single, intense IR mode in the frequency range 320 - 370 cm^{-1} (see Figure 3, and also Table 3). *L*9 is our starting point: this configuration is cubic and characterized by a very intense F_u mode at 347.2 cm^{-1}. In *L*12, trigonal, this triple degenerate mode splits into a double degenerate (E_u) mode at 344.6 cm^{-1} and a singlet (A_u) at 324.2 cm^{-1}. The same situation is found for *L*11, tetragonal, but in this case intensities are smaller. *L*10 is orthorhombic, so that the single mode in *L*9 splits in three singlets at 361.1, 365.9 and 327.4 cm^{-1} (with B_{1u}, B_{2u} and B_{3u} symmetries, respectively). The last three configurations, *L*13, *L*14 and *L*15 display a larger number of modes (the cell is monoclinic or triclinic), so that the link to the original mode is less evident.

We can try to correlate the presence of the peak at about 350 cm^{-1} to the short range Y cation ordering in the cell. To this aim, the first neighbors Y-Y couples were classified as shown in Table

3. Upon symmetry analysis of the end member cubic structure (Mustapha et al. 2012), these couples split in two classes; for each class, the abundance of Fe-Fe, Al-Al and Fe-Al couples is given. The Δ index (see the caption to the Table for the definition) summarizes the relative abundance of heteroatomic and homoatomic couples. $L9$ and $L12$ are configurations where heteroatomic couples are far more abundant than homoatomic couples (Δ_1, Δ_2 are equal to +1, +1 for $L9$ and to +1, 0 for $L12$). In the spectra, both configurations show very intense modes at about 350 cm^{-1}. $L11$ displays a positive Δ_1 but a negative Δ_2 ($\Delta_1 = +1$, $\Delta_2 = -0.33$); also in this case there is a mode at about 350 cm^{-1}, but the intensity is lower than for $L9$ and $L12$. $L10$ presents the largest abundance of homoatomic couples ($\Delta_1 = -1$, $\Delta_2 = +0.33$); in this case there are no intense modes at about 350 cm^{-1}. For the three remaining configurations both Δ_1 and Δ_2 are around zero, and then an intense peak at 350 cm^{-1} cannot be identified. The presence of this peak can then be correlated to the occurrence of a relatively large number of Fe-Al couples. This confirms that structural analysis of short range ordering can be used to support the interpretation of spectroscopic features of binary systems.

Comparison with experiments

A detailed infrared reflectance study on a set of 14 natural garnets belonging to the Adr-Grs binary was carried out in 1995 by McAloon and Hofmeister (McAloon and Hofmeister 1995). In this work the authors presented a Kramers-Kronig analysis of the spectra, based on the hypothesis of quasi-cubic symmetry of the whole series, i.e. 17 modes were searched for each sample; the subsequent mode assignment was made on the assumption of complete decoupling of modes involving different structural subunits. Then, the dependence of IR modes on the composition was classified into two categories: a) one-mode behavior (Lucovsky et al. 1968), in which modes are found along the whole series, showing a linear dependence of ν on the composition; intensity does not vary strongly (thus it is not analyzed in detail in McAloon and Hofmeister 1995). Most of the modes (14 out of 17) were assigned to this class; b) two-mode behavior (Chang and Mitra 1968, Fertel and Perry

1979), according to which there are modes specific to each of the end members: the intensity decreases when going to intermediate compositions, reaching zero when approaching the opposite end member; ν still varies linearly with composition. According to McAloon and Hofmeister 1995, only three modes have a two-mode behavior; they are in the low frequency region and associated to the motion of either FeO_6 (244 and 297 cm^{-1}, Adr) or AlO_6 (425 cm^{-1}, Grs) octahedra. The two-modes behavior was thus expected to be related to local modes (McAloon and Hofmeister 1995), when the substituting atoms show largely different masses or force constants (Chang and Mitra 1968) and when end member bands do not overlap (Fertel and Perry 1979).

We compared the experimental reflectance spectra from McAloon and Hofmeister 1995 with our calculated curves, and observed many similarities in the trends of the modes along the series. In particular, our Lν(2), Hν(3) and Hν(4) bands can be interpreted according to the experimental one-mode behavior. These bands have partial (Lν(2)) or no (the other two) dependence on the substituting Y atoms, resulting in a smooth behavior of frequency on composition. In this respect, the analysis we carried out in the “IR wavenumbers” and “IR intensities” Sections permits to deepen the understanding of these trends, in particular with reference to the intensity, where we discuss the influence of different factors, either structural (cell parameter) or compositional (effect of substituting atoms on mixed modes).

It is worth also comparing the simulated and experimental slopes $d\nu/dx_{Al}$, as a correspondence can be found between the frequencies of our Lν(2), Hν(3) and Hν(4) bands and the ones of modes labelled I, D and B in McAloon and Hofmeister 1995, respectively. In our case, the values are 0.64, 0.36 and 0.37 cm^{-1}/mol% (converted in appropriate units from the “IR wavenumbers” Section), to be compared with 0.67, 0.31 and 0.30 cm^{-1}/mol% from the experiment. The agreement is very satisfactory; in particular, the difference in slope between Ca (Lν(2)) and SiO_4 (Hν(3) and Hν(4)) dominated modes is confirmed.

The case of low frequency, Y cation-specific modes is rather interesting. When comparing the so called two-mode behavior in McAloon and Hofmeister 1995 with our Lν(1) band, we observe in both cases a linear dependence of ν on composition. The significant issue is the different attribution (here and in the experiment) of close-frequency Fe or Al dominated motions to either two separate modes or to the same band. Indeed, both the experimental and the computational descriptions are reasonable, focusing on different aspects of the spectra. Based on the hypotheses of quasi-cubic symmetry and subunits decoupling, experimentalists attempt to perform a complete assignment of all (actually "all 17") modes of the binary. In this respect, simulation unveils aspects of complexity that require to modify this basic assumption in two directions: a) the reduction of symmetry results in a great number of non-degenerate, IR active modes at intermediate compositions (up to 129, *vs* 17 in the end members); b) isotopic substitution shows that different subunits couple together, giving rise to mixed motions, especially in the case of Y cations.

As a consequence of this discussion, it is reasonable to complete the picture of the two-mode behavior with the following remark. On the one hand, when moving towards one end member or the other ($x_{Al} \leq 0.375$ for Adr, or $x_{Al} \geq 0.75$ for Grs), one mode becomes dominant in the Lν(1) frequency range, being associated to motions of the most abundant Y species (either Fe or Al). On the other hand, in the case of intermediate compositions, the same frequency range becomes characterized by a large number of IR active modes (up to 24), that may show a different, and somehow mixed, nature: Fe dominated, Al dominated, or Fe/Al coupled.

CONCLUSIONS

The infrared properties of nine compositions of the andradite-grossular solid solution were computed at the *ab initio* level by using the hybrid B3LYP functional, an all-electron Gaussian-type basis set and the CRYSTAL09 code. The calculations were performed for 23 independent configurations, identified upon symmetry analysis within a primitive cell model.

Infrared bands in the range 700-1000 cm^{-1} (related to Si-O stretchings) show frequencies and intensities anti-correlated and correlated with the Al content, respectively. This behavior is directly related to the linear trend of the cell parameters, and is in agreement with the "one-mode" behavior identified by experimentalists.

Of the two most intense bands identified at low frequencies, the one that spans from 360 (Adr) to 430 (Grs) cm^{-1} is mainly related to Ca motions. Both its frequency and intensity increase linearly with increasing Al content, with a "one-mode" behavior.

The band ranging from 280 (Adr) to 390 (Grs) cm^{-1} corresponds to pure Y cation motions. While the frequency is roughly linearly dependent on composition, the intensity shows a non-constant trend, with a maximum at the Adr side, and a plateau towards the Grs side. This analysis permits a better characterization of the so called "two-mode" behavior in Adr-Grs solid solution. Rather than two single modes with well distinct intensities (Fe and Al specific), a broad band is identified, made up of many modes, whose intensities strongly depend on symmetry and Fe/Al cation-coupling properties.

At fixed binary composition, the Y-specific frequency range (280-390 cm^{-1}) shows a dependence of the spectral features upon short range Y cation ordering. In particular, a peak near 350 cm^{-1} is found, whose intensity depends on the relative abundance of first neighbors Fe-Al heteroatomic couples over Fe-Fe or Al-Al homoatomic ones.

We have shown that *ab initio* calculations are a powerful tool that permits to analyze complex systems such as solid solutions. Relationships among structure and properties are established, so that experimental findings may be critically and robustly interpreted.

ACKNOWLEDGEMENTS

The authors acknowledge Compagnia di San Paolo for financial support (Progetti di Ricerca di Ateneo-Compagnia di San Paolo-2011-Linea 1A, progetto ORTO11RRT5).

FIGURES

Figure 1 Schematic picture of the Adr (Grs) structure: cubic conventional cell and rhombohedral primitive cell. Only the Y sites, containing Fe (Al) atoms, are reported. Labelled sites belong to the conventional cell; among them, shaded sites, labelled from 1 to 8 without primes, belong to the primitive cell. Primed sites are translated images of the corresponding ones in the primitive cell.

Figure 2 Dependence of $\bar{a}=V^{1/3}$ (V is the volume of the conventional cell, in Å^3) on x_{Al}, the fraction of Al atoms in the Y sites per unit cell. For each composition, the dot is the average among the corresponding configurations, and the two bars on each dot refer to the highest and lowest value within the set of corresponding configurations. Note that only for x_{Al} = 0.5 they do not coincide in the figure scale (see also the Volume column in Table 1). The regression line is shown as well.

Figure 3 Calculated infrared spectra for the seven configurations corresponding to x_{Al} = 0.5 (n_{Al} = 4). L and $\mathcal{P}$ are the label of the configuration and the occupation probability at 1300 K and optimized cell volume, respectively, according to Table 1. A Lorentzian function is associated to each calculated frequency (ν); the peak area is the calculated intensity (I); the peak width is set to γ = 9 cm^{-1} (see the "Computational details" Section).

Figure 4 Calculated infrared spectra at 1300 K for nine compositions of the Adr-Grs solid solutions, with x ranging from 0 (Adr) to 1 (Grs), in steps of 0.125 (number of Al atoms n_{Al} = 0-8). Spectra are constructed as in Figure 3. In the case of compositions corresponding to more than one symmetry independent configuration (x = 0.25-0.75), spectra are averaged with $\mathcal{P}$ (the occupation probability of the L^{th} configuration at 1300 K and optimized cell volume) weights, as described in the "Computational details" Section.

Figure 5 Effect of cation isotopic substitution on the calculated spectra at 1300 K of nine compositions of the Adr-Grs solid solutions, with *x* ranging from 0 (Adr) to 1 (Grs), in steps of 0.125 (number of Al atoms n_{Al} = 1-8). Only the low frequency range 200-600 cm^{-1} is plotted. Isotopic spectra are obtained by increasing (Ca) or decreasing (Al and Fe) the masses of the corresponding cations by 20%. Spectra are constructed as in Figure 4.

Figure 6 Infrared properties as a function of x_{Al}, the fraction of Al atoms in the Y sites per unit cell (see also Table 2): (a) wavenumbers ν, and (b) integrated intensities II of the four bands; (c) sum of the infrared intensities $F = \sum_j II_j$. The frequency range is divided in two regions: below (Lν) and above (Hν) 700 cm^{-1}. For each composition, the point and the error bars refer to the average value and to the highest/lowest values, respectively, among the corresponding configurations. The regression line is shown in all cases; note that, for the integrated intensities II of Lν(1) band, two distinct lines are drawn, for the ranges x_{Al} = 0 - 0.375 and x_{Al} = 0.375 - 1, respectively.

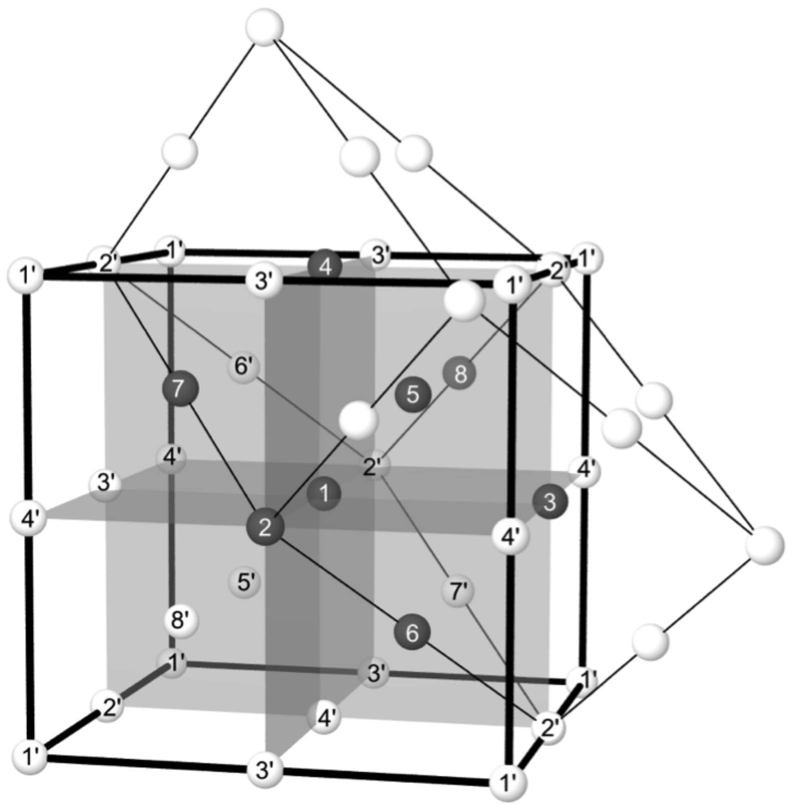

Figure 1

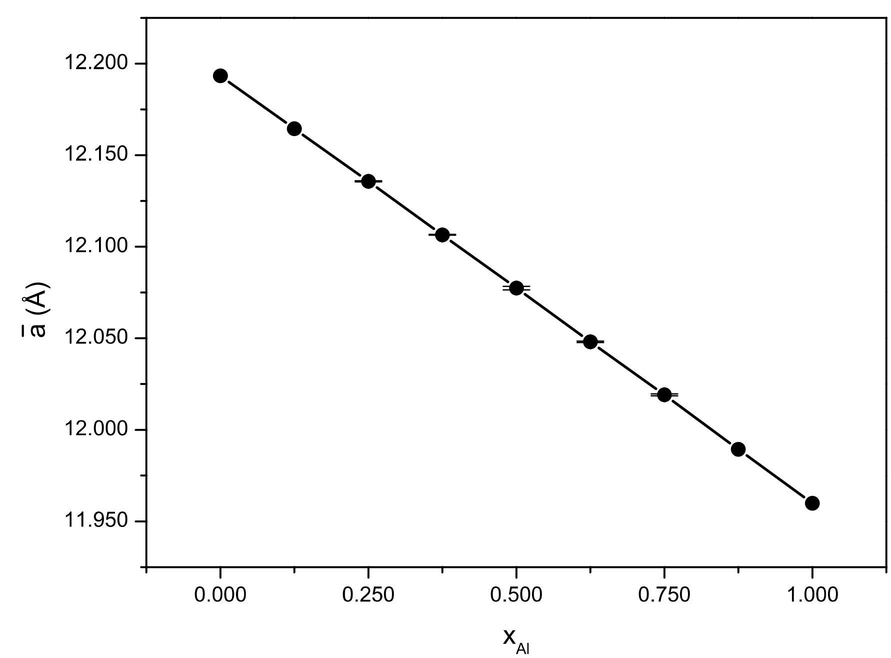

Figure 2

527
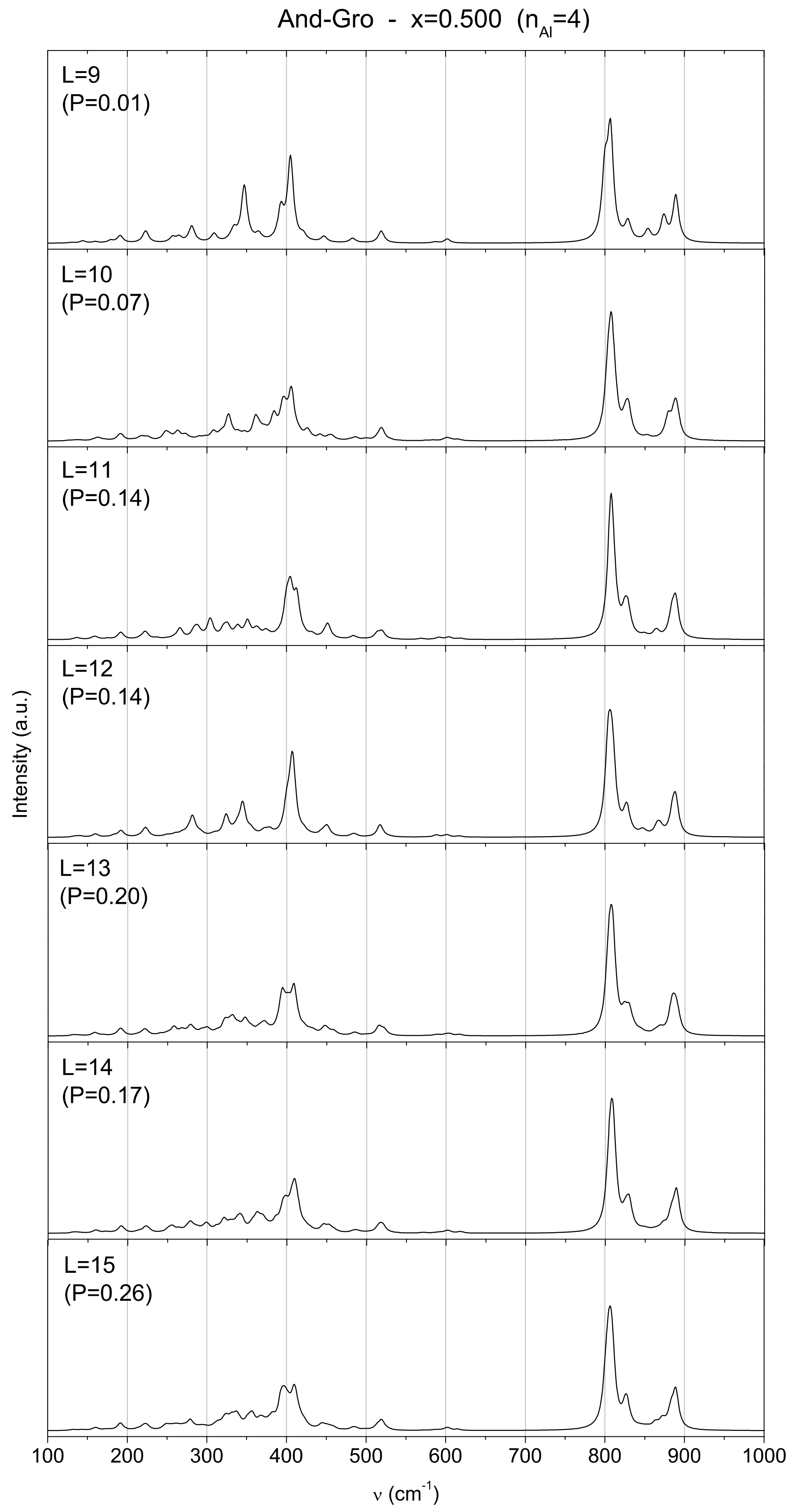

528 **Figure 3**

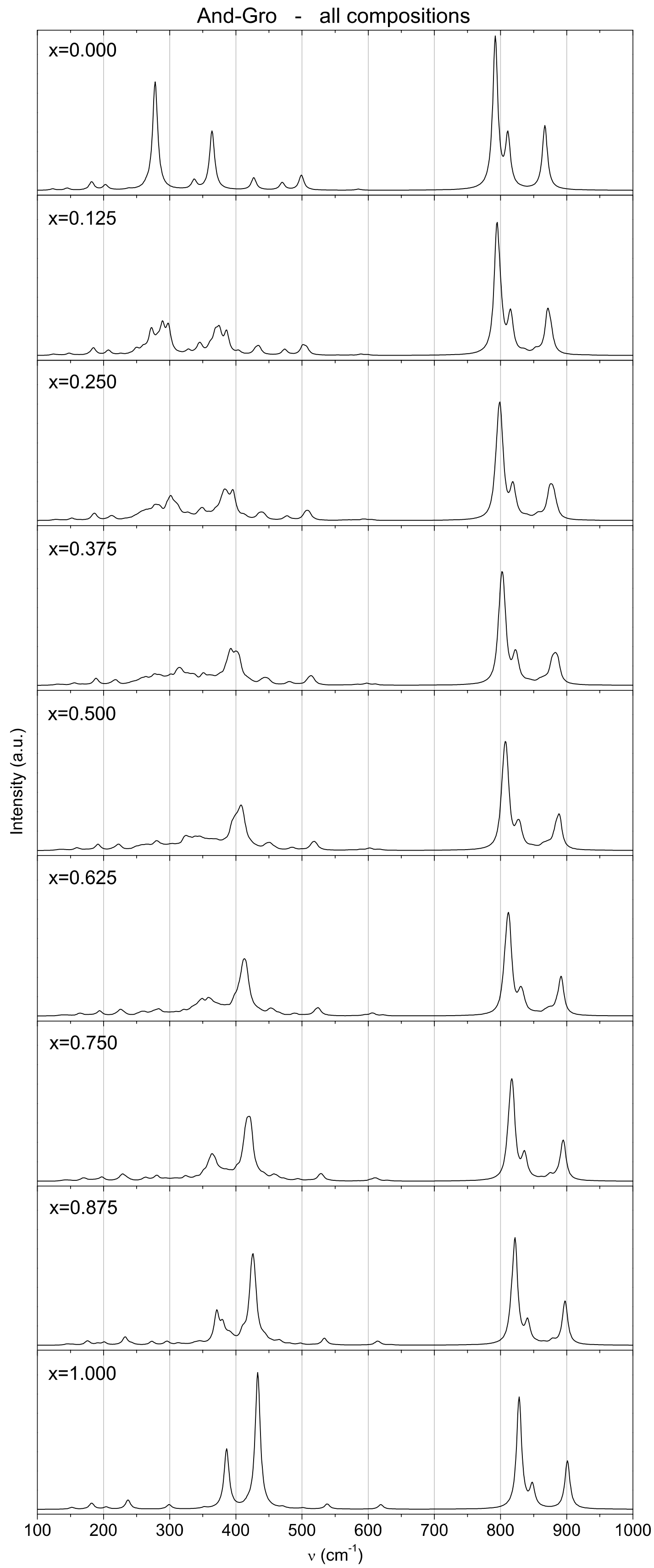

529

530 **Figure 4**

531

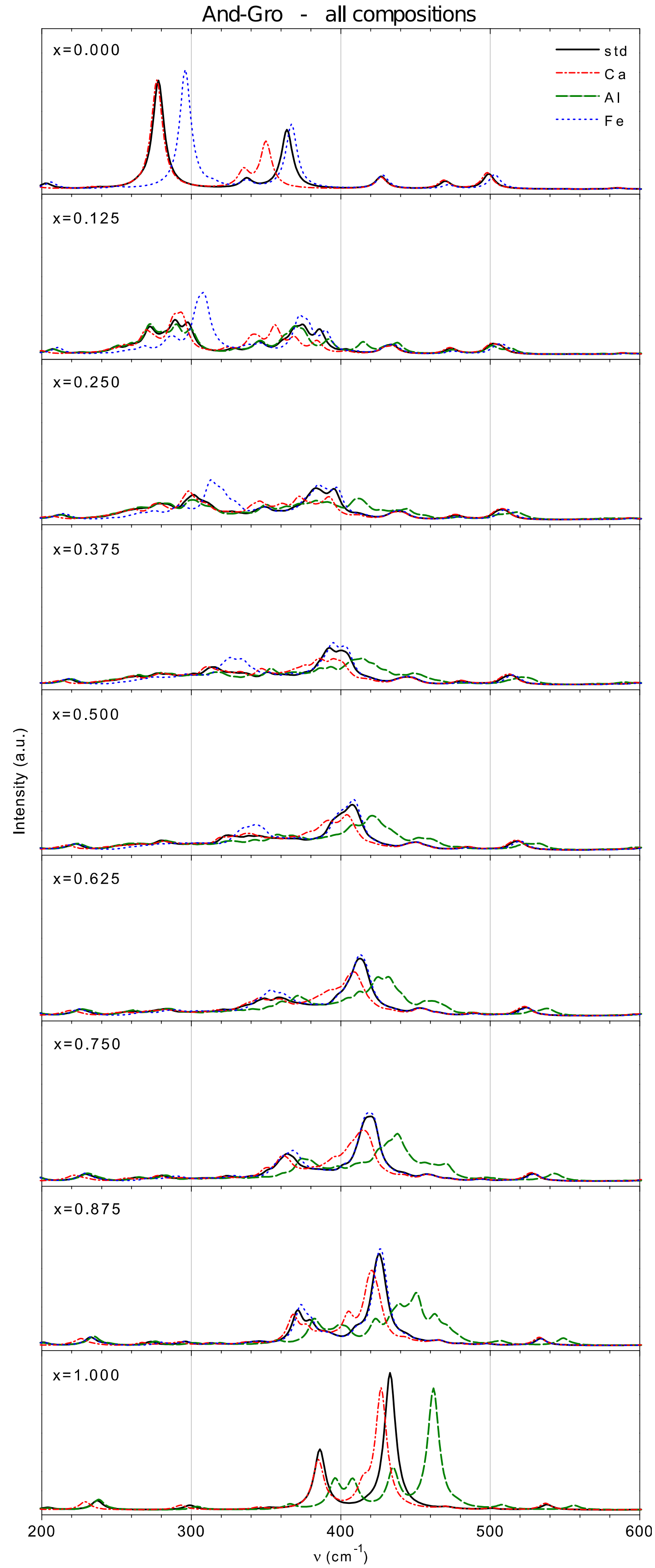

532 **Figure 5**

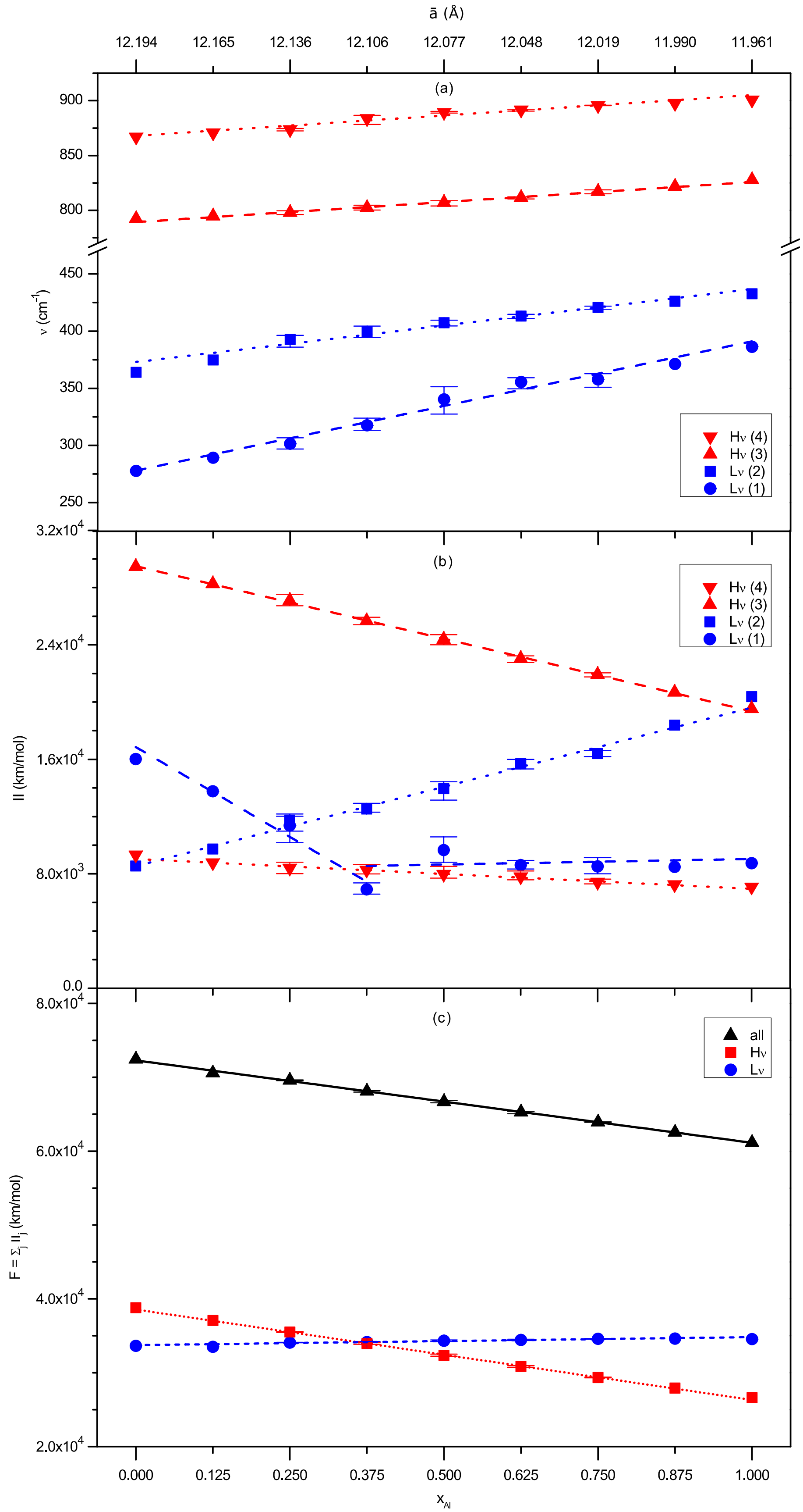
ā (Å)
12.194
12.165
12.136
12.106
12.077
12.048
12.019
11.990
11.961
(a)
ν (cm-1)
Hν (4)
Hν (3)
Lν (2)
Lν (1)
(b)
II (km/mol)
(c)
F = Σj IIj (km/mol)
all
Hν
Lν
0.000
0.125
0.250
0.375
0.500
0.625
0.750
0.875
1.000
xAl

Figure 6

TABLES

n_{Al}	x_{Al}	*L*	$\mathcal{M}$	$\mathcal{S}$	N_{df}	CRY	**D**	*a*	*b*	*c*	α	β	γ	V	$\mathcal{P}$
0	0.000	1	1	48	4	CUB	none	12.193	12.193	12.193	90.000	90.000	90.000	1812.8	1.00
1	0.125	2	8	6	38	TRG	1	12.164	12.164	12.164	89.848	89.848	89.848	1800.0	1.00
2	0.250	3	4	12	19	TRG	1-5	12.136	12.136	12.136	89.706	89.706	89.706	1787.5	0.11
		4	12	4	56	MON	3-4	12.134	12.135	12.137	90.000	90.000	90.293	1787.2	0.37
		5	12	4	57	MON	1-6	12.135	12.138	12.135	89.962	89.673	89.962	1787.2	0.53
3	0.375	6	8	6	38	TRG	5-6-7	12.106	12.106	12.106	89.853	89.853	89.853	1774.3	0.09
		7	24	2	114	TRC	1-2-5	12.105	12.103	12.113	89.850	89.920	89.603	1774.5	0.37
		8	24	2	114	TRC	1-2-7	12.106	12.108	12.104	90.171	89.881	89.880	1774.4	0.54
4	0.500	9	2	24	9	CUB	5-6-7-8	12.077	12.077	12.077	90.000	90.000	90.000	1761.5	0.01
		10	6	8	28	ORT	1-3-5-8	12.086	12.075	12.075	89.383	90.000	90.000	1762.1	0.07
		11	6	8	27	TET	1-2-7-8	12.079	12.079	12.072	90.000	90.000	90.000	1761.3	0.14
		12	8	6	38	TRG	1-6-7-8	12.077	12.077	12.077	89.970	89.970	89.970	1761.5	0.14
		13	12	4	57	MON	1-2-5-7	12.075	12.079	12.079	89.965	89.699	89.699	1761.7	0.20
		14	12	4	57	MON	1-2-5-8	12.074	12.084	12.074	89.732	90.089	89.732	1761.6	0.17
		15	24	2	114	TRC	1-2-3-5	12.080	12.073	12.080	89.704	89.982	89.658	1761.8	0.26
5	0.625	16	8	6	38	TRG	1-2-3-4-8	12.048	12.048	12.048	90.174	90.174	90.174	1748.8	0.08
		17	24	2	114	TRC	3-4-6-7-8	12.048	12.048	12.050	90.137	90.158	90.400	1749.1	0.38
		18	24	2	114	TRC	3-4-5-6-8	12.052	12.042	12.049	89.846	90.069	90.085	1748.7	0.54
6	0.750	19	4	12	19	TRG	2-3-4-6-7-8	12.020	12.020	12.020	90.331	90.331	90.331	1736.5	0.12
		20	12	4	56	MON	1-2-5-6-7-8	12.018	12.018	12.021	90.000	90.000	89.675	1736.2	0.34
		21	12	4	57	MON	2-3-4-5-7-8	12.021	12.021	12.015	90.025	90.025	90.267	1736.1	0.55
7	0.875	22	8	6	38	TRG	2-3-4-5-6-7-8	11.989	11.989	11.989	90.159	90.159	90.159	1723.4	1.00
8	1.000	23	1	48	4	CUB	all	11.960	11.960	11.960	90.000	90.000	90.000	1710.7	1.00

Table 1 Structural properties of the Adr-Grs solid solutions. n_{Al} and x_{Al} are the number and the fraction of Al atoms in the Y sites, respectively; n_{Al} refers to the primitive cell (80 atoms). *L* labels the symmetry independent configurations. $\mathcal{M}$, $\mathcal{S}$ and N_{df} are the multiplicity of each configuration, the number of symmetry operators and the number of geometry variables to be considered in the structure optimization, respectively; CRY indicates the crystal system of the primitive cell, attributed on the basis of the set of symmetry operators. Column **D** indicates the Al atoms of the primitive cell according to the labels of Figure 1. The cell parameters *a*, *b*, *c* [Å], α, β, γ [deg] and V [$Å^3$] are given with reference to the quasi-cubic conventional cell (160 atoms), to facilitate the comparison among configurations. $\mathcal{P}$ is the occupation probability of the L^{th} configuration at 1300 K and optimized cell volume.

			N_{IR}			Lν(1)			Lν(2)			Hν(3)		Hν(4)		F		
n_{Al}	x_{Al}	L	Lν	Hν	all	ν(1)	II(1)	type(1)	ν(2)	II(2)	type(2)	ν(3)	II(3)	ν(4)	II(4)	Lν	Hν	all
0	0.000	1	14	3	17	277.8	16026	Fe	363.9	8542	Ca	792.4	29479	866.9	9323	33636	38802	72437
1	0.125	2	70	16	86	289.2	13766	Fe	374.7	9733	Ca+Al	794.7	28264	870.7	8771	33518	37059	70577
2	0.250	3	53	12	65	296.9	10169	Fe	385.9	12062	Ca+Al	798.0	27530	874.7	8016	34042	35546	69587
		4	105	24	129	306.7	11947	Fe	395.8	12182	Ca+Al	796.2	26735	874.0	8811	34080	35557	69637
		5	105	24	129	301.0	12024	Fe	396.3	10983	Ca+Al	799.7	27042	872.5	8367	34100	35444	69544
3	0.375	6	70	16	86	315.7	6575	Fe	394.4	12924	Ca+Al	804.6	25416	886.6	8643	34125	34064	68188
		7	105	24	129	323.9	7371	Fe	400.1	12304	Ca+Al	802.4	25925	886.1	7990	34224	33921	68145
		8	105	24	129	313.2	6790	Fe	404.4	12359	Ca+Al	800.3	25669	878.2	8164	34132	33864	67996
4	0.500	9	27	6	33	347.2	10074	Al+Fe	404.6	14430	Ca+Al	807.5	23999	888.6	8524	34202	32523	66724
		10	80	18	98	327.4	9549	Al+Fe	406.2	14194	Ca+Al	807.6	24711	889.9	7725	34427	32436	66863
		11	53	12	65	351.3	9818	Al+Fe	405.0	13590	Ca+Al	807.0	24427	889.5	7768	34320	32229	66550
		12	70	16	86	344.6	8804	Al+Fe	407.5	14050	Ca+Al	808.1	24142	888.6	8166	34226	32338	66565
		13	105	24	129	331.8	9612	Al+Fe	409.1	13900	Ca+Al	804.0	24505	890.2	7763	34371	32283	66654
		14	105	24	129	343.0	10577	Al+Fe	409.6	13156	Ca+Al	808.7	24664	889.1	7699	34415	32374	66789
		15	105	24	129	336.6	9167	Al+Fe	409.2	14305	Ca+Al	807.5	24256	889.1	8142	34362	32403	66765
5	0.625	16	70	16	86	357.8	8564	Al+Fe	413.8	15756	Ca+Al	810.4	22773	890.5	8194	34418	30972	65390
		17	105	24	129	359.1	8934	Al+Fe	414.8	15991	Ca+Al	812.1	23232	892.1	7594	34531	30834	65365
		18	105	24	129	349.5	8337	Al+Fe	411.0	15333	Ca+Al	812.2	23123	892.2	7586	34358	30722	65080
6	0.750	19	53	12	65	350.9	8431	Al	420.7	16384	Ca+Al	815.1	22040	895.4	7300	34622	29340	63962
		20	105	24	129	359.4	9127	Al	419.3	16191	Ca+Al	817.4	21765	895.5	7632	34536	29402	63938
		21	105	24	129	362.8	7994	Al	421.9	16620	Ca+Al	818.6	21987	896.0	7322	34590	29316	63906
7	0.875	22	70	16	86	371.2	8487	Al	426.1	18395	Ca+Al	821.8	20688	897.6	7241	34619	27930	62549
8	1.000	23	14	3	17	386.3	8741	Al	432.7	20383	Ca+Al	827.8	19535	900.6	7079	34553	26614	61167

Table 2 Infrared properties of the Adr-Grs solid solutions: overall features and IR bands. n_{Al}, x_{Al} and L as in Table 1. The frequency range is divided

in two regions: below (Lν) and above (Hν) 700 cm^{-1}. N_{IR} is the number of IR-active modes. For each band, ν [cm^{-1}] is the frequency of the most intense mode belonging to the band and II is the integrated intensity [km/mol]. The participation of Ca and Fe/Al cations to the Lν bands is analyzed on the basis of isotopic substitution (see Figure 5); the cations providing the largest contribution to Lν(1) and Lν(2) bands are reported in the "type" column. $F = \sum_j II_j$ is the sum of intensities [km/mol].

L	CRY	Low ν features			Y-Y(1)				Y-Y(2)			
		ν	I	Sym	$n_{Fe\text{-}Fe,1}$	$n_{Al\text{-}Al,1}$	$n_{Fe\text{-}Al,1}$	Δ_1	$n_{Fe\text{-}Fe,2}$	$n_{Al\text{-}Al,2}$	$n_{Fe\text{-}Al,2}$	Δ_2
9	CUB	347.2*	6763	F_u	0	0	8	+1.00	0	0	24	+1.00
10	ORT	361.1	2237	B_{1u}	4	4	0	-1.00	4	4	16	+0.33
		365.9	756	B_{2u}								
		327.4	2360	B_{3u}								
11	TET	351.3*	1975	E_u	0	0	8	+1.00	8	8	8	-0.33
		326.2	1268	A_u								
12	TRG	344.6*	3774	E_u	0	0	8	+1.00	6	6	12	0.00
		324.2	2302	A_u								
13	MON	--	--	--	2	2	4	0.00	6	6	12	0.00
14	MON	--	--	--	2	2	4	0.00	6	6	12	0.00
15	TRC	--	--	--	2	2	4	0.00	4	4	16	+0.33

Table 3 Relationships between IR features in the low frequency region and ordering of Y cations for the seven configurations corresponding to $x_{Al} = 0.5$ ($n_{Al} = 4$). L is the label of the configuration. CRY indicates the crystal system of the primitive cell. ν, I and Sym are the frequency [cm^{-1}], intensity [km/mol] and symmetry, respectively, of the most intense IR modes lying in the interesting frequency range 320-370 cm^{-1} (see discussion in the "Behavior at fixed composition" Section). In the case of L13, L14 and L15 it is not possible to unambiguously identify single intense modes in this range. First neighbors Y cations lie at a distance of about 5.2 Å. According to symmetry analysis, the first neighbors Y-Y couples are classified into two inequivalent classes (columns "Y-Y(1)" and "Y-Y(2)"); $n_{Fe\text{-}Fe}$, $n_{Al\text{-}Al}$ and $n_{Fe\text{-}Al}$ are the numbers of couples of the three different kinds. The total number of couples per unit cell, i.e. $N_{Y\text{-}Y} = n_{Fe\text{-}Fe} + n_{Al\text{-}Al} + n_{Fe\text{-}Al}$, is 8 and 24 for the two classes, respectively. $\Delta = [n_{Fe\text{-}Al} - (n_{Fe\text{-}Fe} + n_{Al\text{-}Al})]/N_{Y\text{-}Y}$ is an indicator of the relative abundance of heteroatomic ($\Delta > 0$) or homoatomic ($\Delta < 0$) couples in each configuration. *Modes near 350 cm^{-1}: see the "Behavior at fixed composition" Section.

References

Akizuki, M. (1984) Origin of Optical Variations in Grossular-Andradite Garnet. American Mineralogist, 69, 328–338.

Andrut, M. and Wildner, M. (2001) The crystal chemistry of birefringent natural uvarovites: Part I. Optical investigations and UV-VIS-IR absorption spectroscopy. American Mineralogist, 86, 1219–1230.

Barrow, G. M. (1962) Introduction to molecular spectroscopy. McGraw-Hill, New York.

Becke, A. D. (1993) Density functional theochemistry. III The role of exact exchange. Journal of Chemical Physics, 98, 5648–5652.

Becker, U. and Pollok, K. (2002) Molecular simulations of interfacial and thermodynamic mixing properties of grossular-andradite garnets. Physics and Chemistry of Minerals, 29, 52–64.

Bosenick, A., Dove, M. T., and Geiger, C. A. (2000) Simulation studies on the pyrope-grossular garnet solid solution. Physics and Chemistry of Minerals, 27, 398–418.

Broyden, C. G. (1970) The Convergence of a Class of Double-rank Minimization Algorithms 1. General Considerations. Journal of the Institute of Mathematics and its Applications, 6, 76–90.

Chang, I. F. and Mitra, S. S. (1968) Applications of a modified long-range iso-displacement model to long-wavelength optic phonons of mixed crystals. Physical Review, 172, 924–933.

Chiriu, D., Ricci, P. C., Carbonaro, C. M., Anedda, A., Aburish-Hmidat, M., Grosu, A., Lorrai, P. G., and Fortin, E. (2006) Vibrational properties of mixed $(Y_3Al_5O_{12})(x)$-$(Y_3Sc_2Ga_3O_{12})(1-x)$ crystals. Journal of Applied Physics, 100, 033101.

Civalleri, B., D'Arco, Ph., Orlando, R., Saunders, V. R., and Dovesi, R. (2001) Hartree-Fock geometry optimization of periodic system with the CRYSTAL code. Chemical Physics Letters, 348, 131–138.

Connolly, J. W. D. and Williams, A. R. (1983) Density-Functional Theory Applied to Phase-Transformations in Transition-Metal Alloys. Physical Review B, 27, 5169–5172.

Dall'Olio, S., Dovesi, R., and Resta, R. (1997) Spontaneous polarization as a Berry phase of the

Hartree-Fock wave function: The case of $KNbO_3$. Physical Review B, 56, 10105–10114.

Deer, W., Howie, R., and Zussman, J. (1992) An introduction to the rock forming minerals. John Wiley, New York.

Demichelis, R., Noël, Y., Ugliengo, P., Zicovich-Wilson, C. M., and Dovesi, R. (2011) Physico-Chemical Features of Aluminum Hydroxides As Modeled with the Hybrid B3LYP Functional and Localized Basis Functions. Journal of Physical Chemistry C, 115, 13107–13134.

Doll, K. (2001) Implementation of analytical Hartree-Fock gradients for periodic systems. Computer Physics Communications, 137, 74–88.

Doll, K., Harrison, N. M., and Saunders, V. R. (2001) Analytical Hartree-Fock gradients for periodic systems. International Journal of Quantum Chemistry, 82, 1–13.

Dovesi, R., Saunders, V. R., Roetti, C., Orlando, R., Zicovich-Wilson, C. M., Pascale, F., Doll, K., Harrison, N. M., Civalleri, B., Bush, I. J., D'Arco, Ph., and Llunell, M. (2009) CRYSTAL09 User's Manual. Università di Torino, Torino, Italy.

Dovesi, R., De La Pierre, M., Ferrari, A. M., Pascale, F., Maschio, L., and Zicovich-Wilson, C. M. (2011) The IR vibrational properties of six members of the garnet family: a quantum mechanical ab initio study. American Mineralogist, 96, 1787–1798.

Fertel, J. H. and Perry, C. H. (1979) Optical phonons in $KCl_{1-x}Br_x$ and $K_{1-x}Rb_xI$ mixed crystals. Physical Review, 184, 874–884.

Fletcher, R. (1970) A new approach to variable metric algorithms. Computer Journal, 13, 317–322.

Freeman, C. L., Allan, N. L., and van Westrenen, W. (2006) Local cation environments in the pyrope-grossular Mg(3)Al(2)Si(3)O(12)-Ca(3)Al(2)Si(3)O(12) garnet solid solution. Physical Review B, 74, 134203.

Geiger, C. A. (1998) A powder infrared spectroscopic investigation of garnet binaries in the system $Mg_3Al_2Si_3O_{12}$-$Fe_3Al_2Si_3O_{12}$-$Mn_3Al_2Si_3O_{12}$-$Ca_3Al_2Si_3O_{12}$. European Journal of Mineralogy, 10, 407–422.

Geiger, C. A., Winkler, B., and Langer, K. (1989) Infrared spectra of synthetic almandine-grossular and almandine-pyrope garnet solid solutions. Mineralogical Magazine, 53, 231–237.

Goldfarb, D. (1970) A Family of Variable-Metric Methods Derived by Variational Means. Mathematics of Computation, 24, 23–26.

Hess, B. A., Schaad, L. J., Carsky, P., and Zahradnik, R. (1986) Ab Initio Calculations of Vibrational Spectra and Their Use in the Identification of Unusual Molecules. Chemical Reviews, 86, 709–730.

Hofmeister, A. M. and Chopelas, A. (1991) Vibrational spectroscopy of end-member silicate garnets. Physics and Chemistry of Minerals, 17, 503–526.

Hofmeister, A. M., Fagan, T. J., Campbell, K. M., and Schaal, R. B. (1996) Single-crystal IR spectroscopy of pyrope-almandine garnets with minor amounts of Mn and Ca. American Mineralogist, 81, 418–428.

Hofmeister, A. M., Schaal, R. B., Campbell, K. M., Berry, S. L., and Fagan, T. J. (1998) Prevalence and origin of birefringence in 48 garnets from the pyrope-almandine-grossularite-spessartine quaternary. American Mineralogist, 83, 1293–1301.

Hofmeister, A. M., Giesting, P. A., Wopenka, B., Gwanmesia, G. D., and Jolliff, B. L. (2004) Vibrational spectroscopy of pyrope-majorite garnets: Structural implications. American Mineralogist, 89, 132–146.

Isaak, D. G. and Graham, E. K. (1976) Elastic Properties of an Almandine Spessartine Garnet and Elasticity in Garnet Solid-Solution Series. Journal of Geophysical Research, 81, 2483–2489.

Isaak, D. G., Anderson, O. L., and Oda, H. (1992) High-Temperature Thermal-Expansion and Elasticity of Calcium-Rich Garnets. Physics and Chemistry of Minerals, 19, 106–120.

Koch, W. and Holthausen, M. C. (2000) A Chemist's Guide to Density Functional Theory. Wiley-VCH Verlag GmbH, Weinheim, Germany.

Kolesov, B. A. and Geiger, C. A. (1998) Raman Spectra of Silicate Garnets. Physics and Chemistry of Minerals, 25, 142–151.

Laks, D. B., Ferreira, L. G., Froyen, S., and Zunger, A. (1992) Efficient Cluster-Expansion for

Substitutional Systems. Physical Review B, 46, 12587–12605.

Lucovsky, G., Brodsky, M., and Burstein, E. (1968) Optical lattice modes in mixed polar crystals, pages 592–601. Plenum Press, New York.

McAloon, B. P. and Hofmeister, A. M. (1995) Single-crystal IR spectroscopy of grossular-andradite garnets. American Mineralogist, 80, 1145–1156.

Merli, M., Callegari, A., Cannillo, E., Caucia, F., Leona, M., Oberti, R., and Ungaretti, L. (1995) Crystal-chemical complexity in natural garnets: Structural constraints on chemical variability. Europen Journal of Mineralogy, 7, 1239–1249.

Meyer, A., D'Arco, Ph., Orlando, R., and Dovesi, R. (2009) Andradite-Uvarovite Solid Solutions. An ab Initio All-Electron Quantum Mechanical Simulation with the CRYSTAL06 Code. Journal of Physical Chemistry C, 113, 14507–14511.

Meyer, A., Pascale, F., Zicovich-Wilson, C. M., and Dovesi, R. (2010) Magnetic Interactions and Electronic Structure of Uvarovite and Andradite Garnets. An Ab Initio All-Electron Simulation With the CRYSTAL06 Program. International Journal of Quantum Chemistry, 110, 338–351.

Moreira, I. D. R. and Dovesi, R. (2004) Periodic approach to the electronic structure and magnetic coupling in $KCuF_3$, K_2CuF_4, and $Sr_2CuO_2Cl_2$ low-dimensional magnetic systems. International Journal of Quantum Chemistry, 99, 805–823.

Moreira, I. D. R., Illas, F., and Martin, R. L. (2002) Effect of Fock exchange on the electronic structure and magnetic coupling in NiO. Physical Review B, 65, 155102.

Muñoz, D., Harrison, N. M., and Illas, F. (2004) Electronic and magnetic structure of $LaMnO_3$ from hybrid periodic density-functional theory. Physical Review B, 69, 085115.

Mustapha, S., D'Arco, Ph., De La Pierre, M., Noël, Y., Ferrabone, M., and Dovesi, R. (2012) On the use of symmetry in the configurational analysis for the simulation of disordered solids. Submitted to Journal of Physics: Condensed Matter.

Noël, Y., Zicovich-Wilson, C. M., Civalleri, B., D'Arco, Ph., and Dovesi, R. (2002) Polarization properties of ZnO and BeO: an ab initio study through the Berry phase and Wannier functions approaches. Physical Review B, 65, 014111.

Olson, D. W. (2001) Garnet, Industrial. U.S. Geological survey minerals yearbook, 30.1-30.4.

O'Neill, B., Bass, J. D., Smyth, J. R., and Vaughan, M. T. (1989) Elasticity of a Grossular-Pyrope-Almandine Garnet. Journal of Geophysical Research, 94, 17819–17824.

Papagelis, K., Arvanitidis, J., Vinga, E., Christofilos, D., Kourouklis, G. A., Kimura, H., and Ves, S. (2010) Vibrational properties of (Gd(1- x)Y(x))(3)Ga(5)O(12) solid solutions. Journal of Applied Physics, 107, 113504.

Pascale, F., Zicovich-Wilson, C. M., López Gejo, F., Civalleri, B., Orlando, R., and Dovesi, R. (2004) The calculation of the vibrational frequencies of the crystalline compounds and its implementation in the CRYSTAL code. Journal of Computational Chemistry, 25, 888–897.

Pascale, F., Catti, M., Damin, A., Orlando, R., Saunders, V. R., and Dovesi, R. (2005) Vibration frequencies of $Ca_3Fe_2Si_3O_{12}$ andradite. An ab initio study with the CRYSTAL code. Journal of Physical Chemistry B, 109, 18522–18527.

Patterson, C. H. (2008) Small polarons and magnetic antiphase boundaries in $Ca_{2-x}Na_xCuO_2Cl_2$ (x=0.06, 0.12): Origin of striped phases in cuprates. Physical Review B, 77, 094523.

Prencipe, M., Pascale, F., Zicovich-Wilson, C. M., Saunders, V. R., Orlando, R., and Dovesi, R. (2004) The vibrational spectrum of calcite ($CaCO_3$): an ab initio quantum mechanical calculation. Physics and Chemistry of Minerals, 31, 559–564.

Rickwood, P. C. (1968) On recasting analyses of garnet into end-member molecules. Contributions to Mineralogy and Petrology, 18, 175–198.

Shanno, D. F. (1970) Conditioning of quasi-Newton methods for function minimization. Mathematics of Computation, 24, 647–656.

Shannon, R. D. (1976) Revised Effective Ionic Radii and Systematic Studies of Interatomic Distances in Halides and Chalcogenides. Acta Crystallographica, A32, 751–767.

Sluiter, M. H. F. and Kawazoe, Y. (2003) Cluster expansion method for adsorption: Application to hydrogen chemisorption on graphene. Physical Review B, 68, 085410.

Sluiter, M. H. F., Vinograd, V., and Kawazoe, Y. (2004) Intermixing tendencies in garnets: Pyrope and grossular. Physical Review B, 70, 184120.

van Westrenen, W., Allan, N. L., Blundy, J. D., Lavrentiev, M. Y., Lucas, B. R., and Purton, J. A. (2003) Trace element incorporation into pyrope-grossular solid solutions: an atomistic simulation study. Physics and Chemistry of Minerals, 30, 217–229.

Vinograd, V. L. and Sluiter, M. H. F. (2006) Thermodynamics of mixing in pyrope-grossular, $Mg_3Al_2Si_3O_{12}$-$Ca_3Al_2Si_3O_{12}$, solid solution from lattice dynamics calculations and Monte Carlo simulations. American Mineralogist, 91, 1815–1830.

Vinograd, V. L., Sluiter, M. H. F., Winkler, B., Putnis, A., Halenius, U., Gale, J. D., and Becker, U. (2004) Thermodynamics of mixing and ordering in pyrope-grossular solid solution. Mineralogical Magazine, 68, 101–121.

Vinograd, V. L., Winkler, B., Putnis, A., Kroll, H., Milman, V., Gale, J. D., and Fabrichnaya, O. B. (2006) Thermodynamics of pyrope-majorite, $Mg_3Al_2Si_3O_{12}$-$Mg_4Si_4O_{12}$, solid solution from atomistic model calculations. Molecular Simulation, 32, 85–99.

Wildner, M. and Andrut, M. (2001) The crystal chemistry of birefringent natural uvarovites: Part II. Single-crystal X-ray structures. American Mineralogist, 86, 1231–1251.

Yu, Y. G., Wentzcovitch, R. M., Vinograd, V. L., and Angel, R. J. (2011) Thermodynamic properties of $MgSiO_3$ majorite and phase transitions near 660 km depth in $MgSiO_3$ and Mg_2SiO_4: A first principles study. Journal of Geophysical Research, 116, B02208.

Zicovich-Wilson, C. M., Pascale, F., Roetti, C., Orlando, R., Saunders, V. R., and Dovesi, R. (2004) Calculation of the vibration frequencies of alpha-quartz: The effect of Hamiltonian and basis set. Journal of Computational Chemistry, 25, 1873–1881.

Zicovich-Wilson, C. M., Torres, F. J., Pascale, F., Valenzano, L., Orlando, R., and Dovesi, R. (2008) Ab initio Simulation of the IR Spectra of Pyrope, Grossular and Andradite. Journal of Computational Chemistry, 29, 2268–2278.

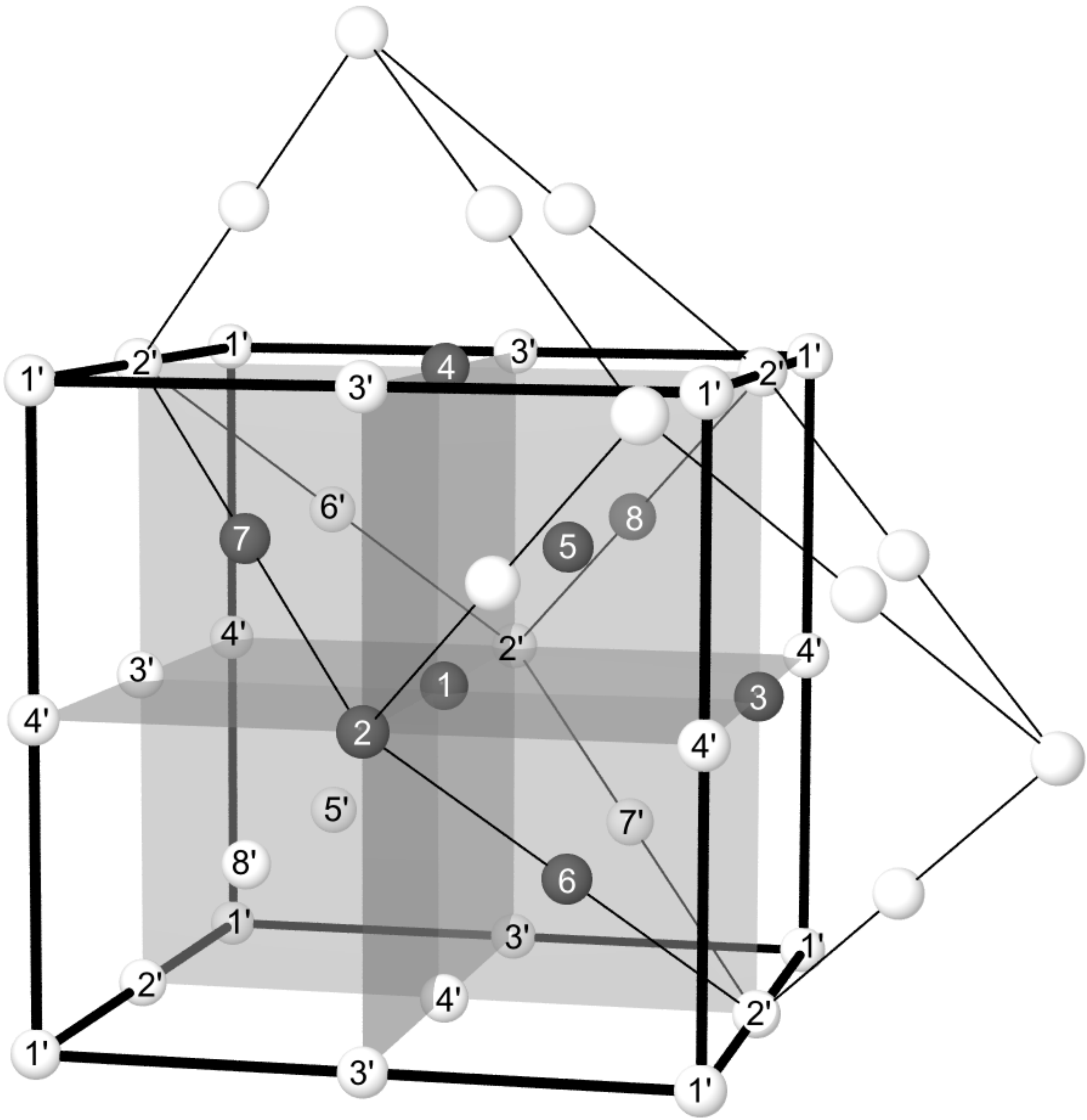
1'
2'
1'
3'
4
3'
2'
1'
1'
6'
7
8
5
4'
2'
3'
1
3
4'
4'
2
4'
5'
7'
8'
6
1'
3'
1'
2'
4'
2'
1'
3'
1'

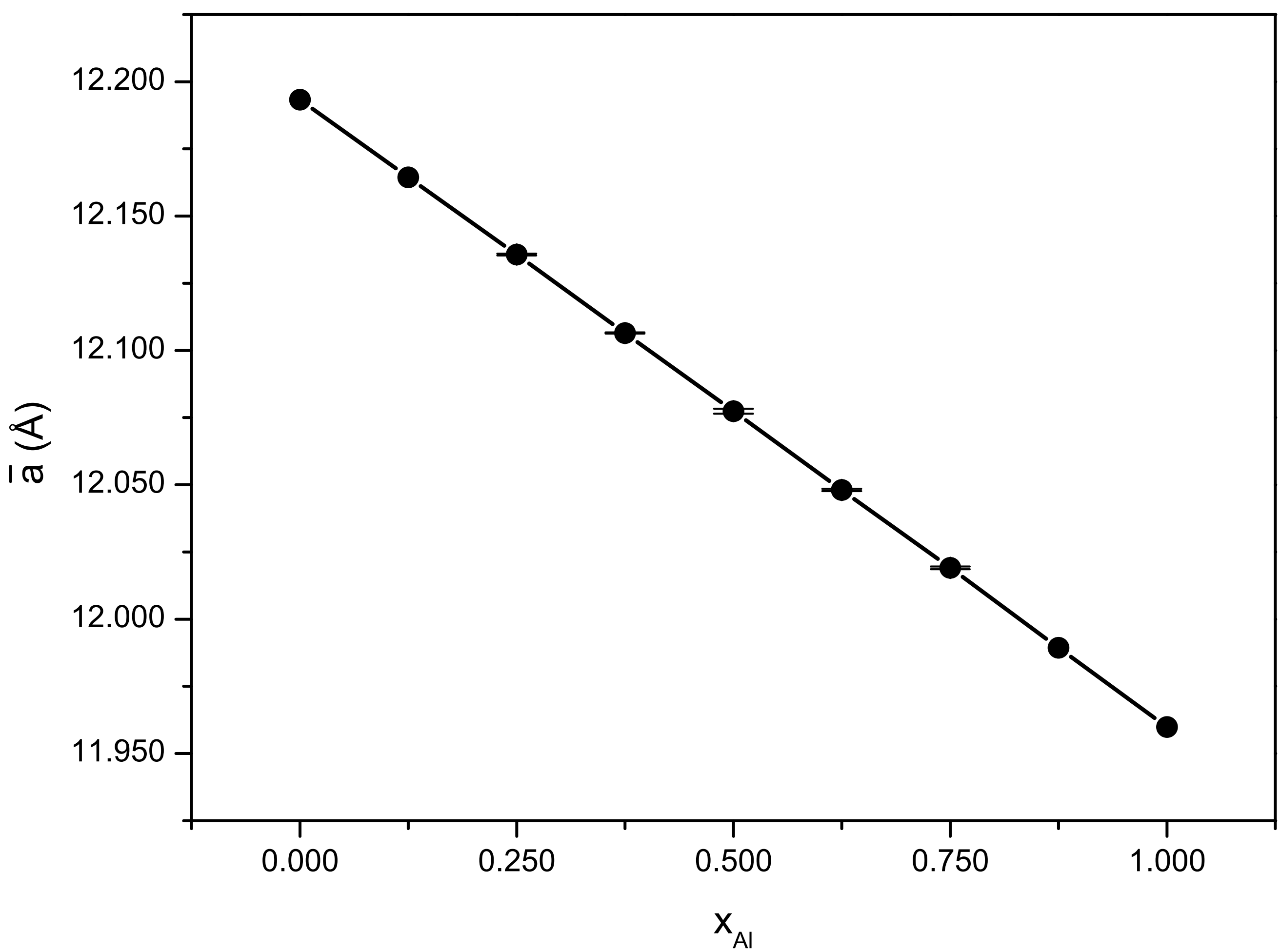

12.200
12.150
12.100
12.050
12.000
11.950
ā (Å)
0.000
0.250
0.500
0.750
1.000
x_Al

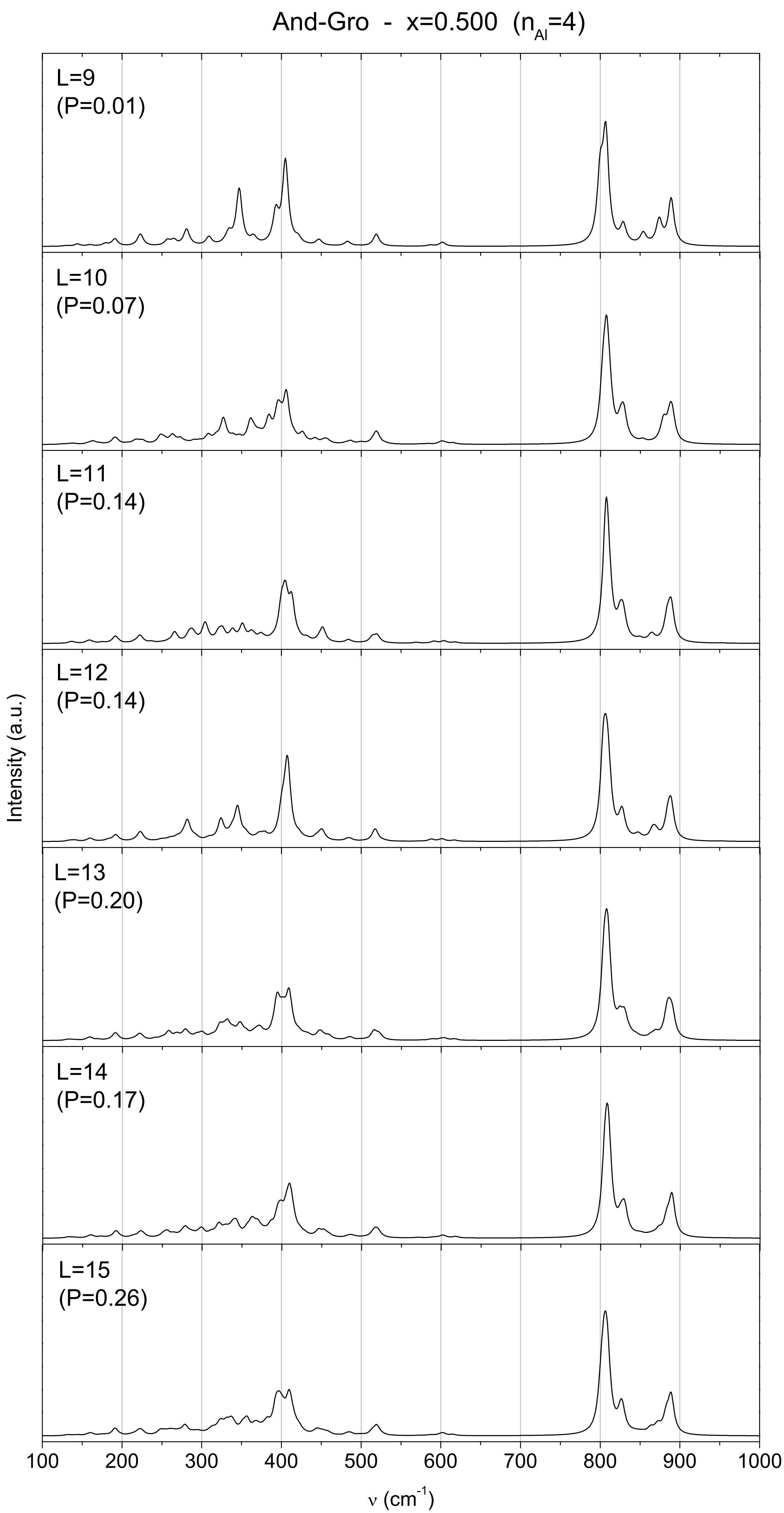

And-Gro - x=0.500 (n_{Al}=4)
L=9
(P=0.01)
L=10
(P=0.07)
L=11
(P=0.14)
L=12
(P=0.14)
L=13
(P=0.20)
L=14
(P=0.17)
L=15
(P=0.26)
Intensity (a.u.)
100 200 300 400 500 600 700 800 900 1000
ν (cm^{-1})

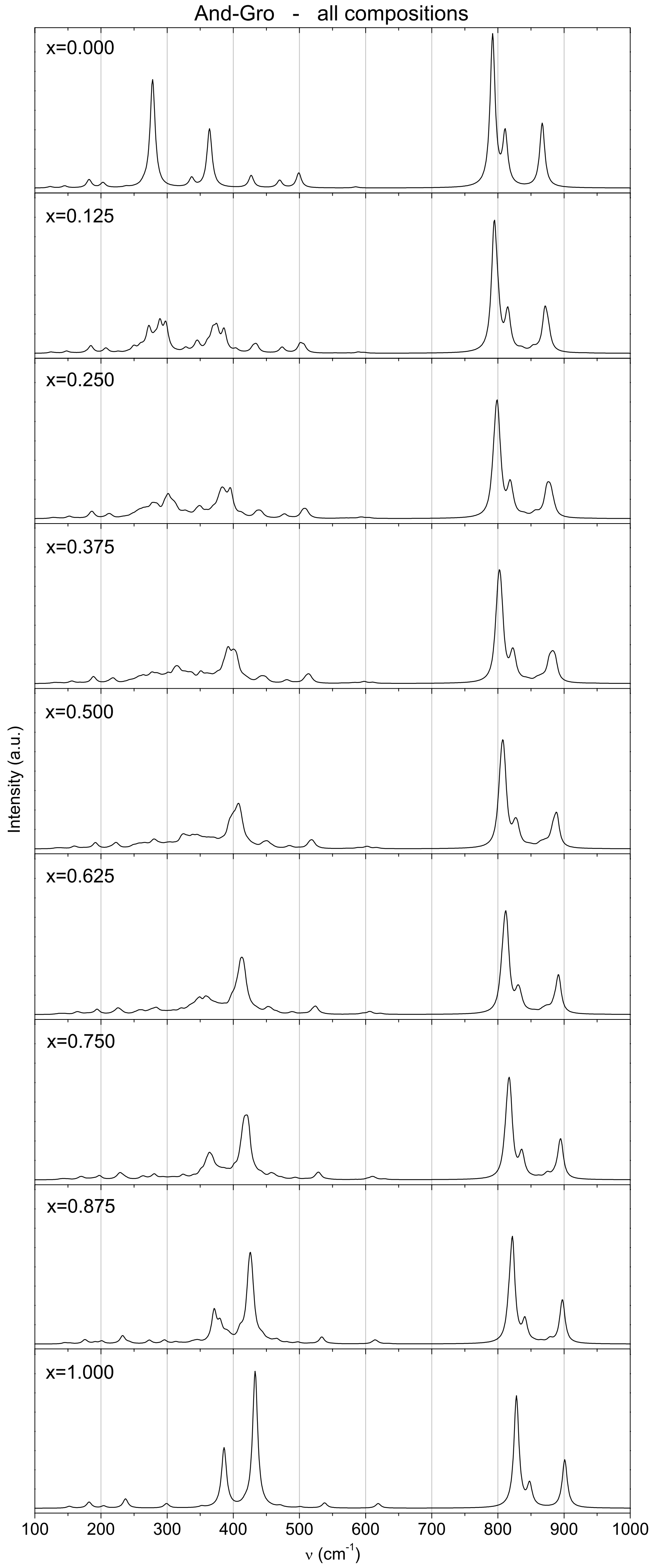
And-Gro - all compositions
x=0.000
x=0.125
x=0.250
x=0.375
x=0.500
x=0.625
x=0.750
x=0.875
x=1.000
Intensity (a.u.)
100
200
300
400
500
600
700
800
900
1000
ν (cm-1)

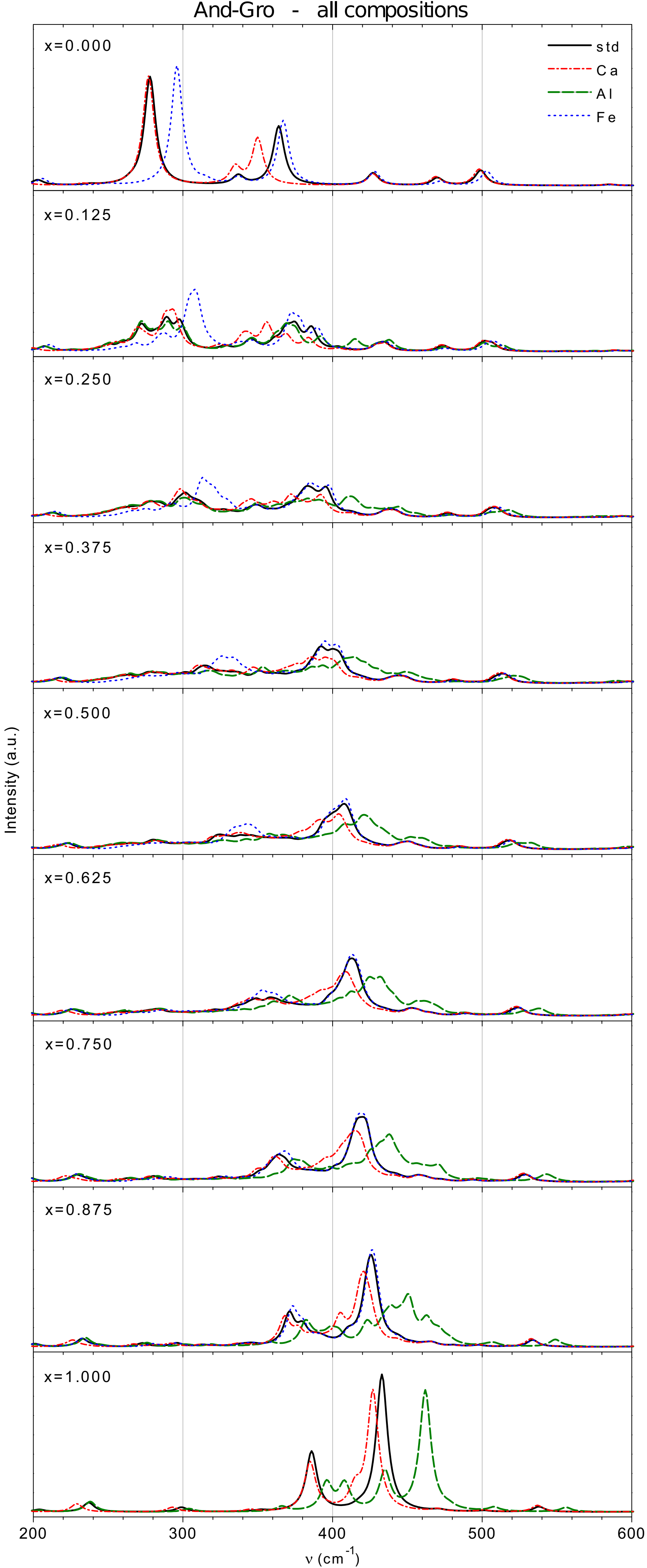
And-Gro - all compositions
std
Ca
Al
Fe
x=0.000
x=0.125
x=0.250
x=0.375
x=0.500
x=0.625
x=0.750
x=0.875
x=1.000
Intensity (a.u.)
200
300
400
500
600
ν (cm^{-1})

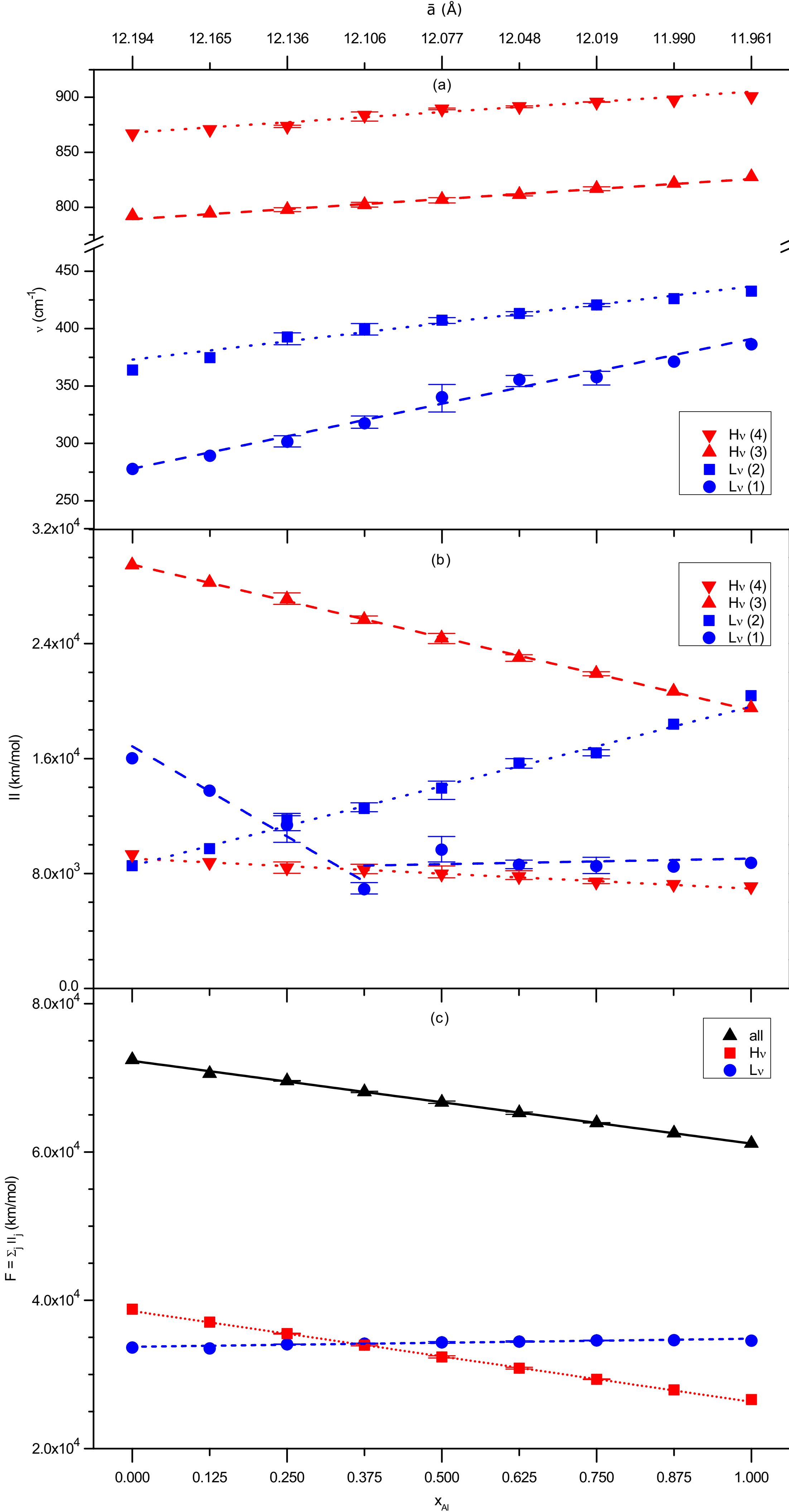

ā (Å)
12.194
12.165
12.136
12.106
12.077
12.048
12.019
11.990
11.961
(a)
900
850
800
450
400
350
300
250
ν (cm-1)
Hν (4)
Hν (3)
Lν (2)
Lν (1)
3.2x10^4
(b)
2.4x10^4
1.6x10^4
8.0x10^3
0.0
II (km/mol)
Hν (4)
Hν (3)
Lν (2)
Lν (1)
8.0x10^4
(c)
6.0x10^4
4.0x10^4
2.0x10^4
F = Σj IIj (km/mol)
all
Hν
Lν
0.000
0.125
0.250
0.375
0.500
0.625
0.750
0.875
1.000
xAl